Synergistic enhancement of PEM fuel cell performance for heavy-duty applications: PtCo/N-doped carbon catalyst and short-side-chain ionomer integration

Journal of Power Sources xxx (xxxx) xxx

Contents lists available at ScienceDirect

Journal of Power Sources

journal homepage: www.elsevier.com/locate/jpowsour

Synergistic enhancement of PEM fuel cell performance for heavy-duty applications: PtCo/N-doped carbon catalyst and short-side-chain ionomer integration

Maria Chiara Massaro [a], Giovanni Marco Carrabba [a], Enrico Sartoretti [a], Anna Ostroverkh [b], Fiora Artusio [a], Roberto Pisano [a], Ulrike I. Kramm [b], Alessandro Hugo Antonio Monteverde [a,*]

[a] Politecnico di Torino, Department of Applied Science and Technology, Corso Duca degli Abbruzzi, 24, 10129, Torino, Italy
[b] Technische Universität Darmstadt, Department of Chemistry, Otto-Berndt-Str. 3, 64287, Darmstadt, Germany

HIGHLIGHTS

- PtCo/N-doped carbon shows >16 × higher mass activity than commercial Pt/Vulcan.
- Mesoporous N-doped support enhances ECSA, Pt utilization, and oxygen transport.
- PtCo catalyst outperforms Pt/Vulcan at 2 bar(abs), revealing pressure dependence.
- Short-side-chain PFSA ionomer improves PEMFC performance at low humidity (33–50% RH).
- EIS confirms reduced ohmic and charge-transfer resistances versus baseline MEA.

GRAPHICAL ABSTRACT

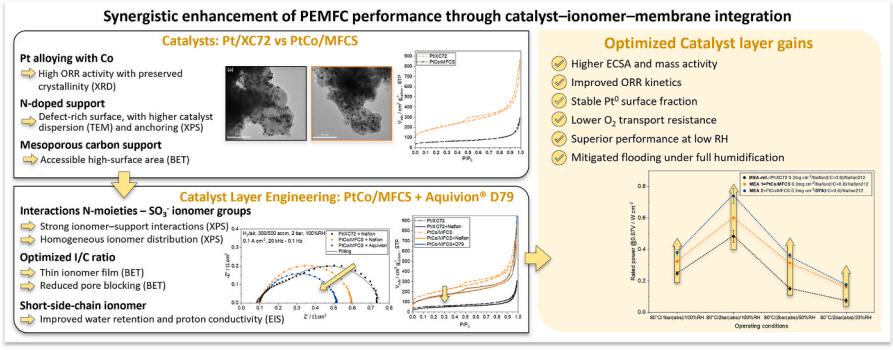

ABSTRACT

This study systematically investigates a synergistic catalyst–ionomer design strategy integrating catalyst architecture, support chemistry, and ionomer structure to enable proton exchange membrane fuel cell (PEMFC) performance relevant to heavy-duty applications. A non-commercial PtCo alloy catalyst supported on nitrogen-doped mesoporous carbon (PtCo/MFCS) enhances intrinsic oxygen reduction reaction activity via alloying while promoting ionomer dispersion, proton accessibility, and favorable interfacial interactions through surface nitrogen functionalities. In parallel, a short-side-chain perfluorosulfonic acid (SSC PFSA) ionomer (Aquivion® D79) is introduced to improve proton conductivity and water retention under low-humidity conditions. In a systematic MEA campaign, PtCo/MFCS delivers over 16 × higher mass activity at 0.9 V (537 vs 32 mA mg_{Pt}^{-1}) than a commercial Pt/Vulcan catalyst, despite 43% lower Pt loading, supported by higher electrochemically active surface area and improved dispersion. Beyond kinetic gains, the mesoporous nitrogen-doped support enhances mid-to-high current density performance by facilitating oxygen transport and water management. Replacing Nafion® with Aquivion® D79 further sustains performance under partial humidification down to 33% RH, demonstrating that SSC ionomer benefits emerge only when coupled with appropriate support porosity and chemistry. Overall, the results reveal strong catalyst–support–ionomer synergy, enabling robust, balance-of-plant-friendly PEMFC operation and offering a credible pathway toward U.S. Department of Energytargets for heavy-duty fuel cell.

* Corresponding author.
E-mail address: alessandro.monteverdevidela@polito.it (A.H.A. Monteverde).

https://doi.org/10.1016/j.jpowsour.2026.239323
Received 13 October 2025; Received in revised form 23 December 2025; Accepted 9 January 2026

1. Introduction

Proton Exchange Membrane Fuel Cells (PEMFCs) are a leading candidate for decarbonizing heavy-duty transportation due to their potential for high power density and efficiency.

Their performance and durability, however, are largely dictated by the Membrane Electrode Assembly (MEA), which comprises a polymer electrolyte membrane sandwiched between the anode and cathode catalyst layers (CLs), which are in turn supported by respective gas diffusion layers (GDLs) on each side [1,2].

Although progress in membrane structure and configuration continues to enhance proton transport and thermal stability [3], the decisive advances in PEMFCs will stem from catalyst layer engineering, where improvements in both electrocatalytic activity and mass transport directly govern overall cell performance [2,4]. The CLs within the MEA are meticulously designed to maximize electrochemical reaction efficiency at the triple phase boundary (TPB) — where protons, electrons, and reactant gases meet [5]. The conventional architecture relies on platinum nanoparticles dispersed on carbon supports and coated with thin ionomer films, providing the pathways for proton conduction and gas diffusion [6]. Advances aim to reduce platinum usage by optimizing deposition techniques [7], alloying strategies to enhance electrocatalytic activity [8], or developing alternative catalysts [9–13], as the cost and scarcity of platinum remain significant barriers to scalability [6].

Reaching the U.S. Department of Energy (DOE) target for heavy-duty of 8.5 kW L^{-1} power density [14] demands significant advancements in both catalyst activity and CL design. Research priorities in this area cover: (1) high-activity catalysts not restricted by ultra-low platinum-group metal (PGM) levels [1,15,16], (2) stability of catalysts and ionomers at temperatures exceeding 90–100 °C [17,18], (3) durability of ionomers and membranes under low-humidity conditions [19,20], and (4) robust catalysts, supports, and membranes [3]. Furthermore, considerations about recyclability of materials and their compatibility with existing production lines should be considered.

For light-duty vehicles (LDVs), optimization focuses on minimizing resistance and maximizing current density. In contrast, heavy-duty vehicles (HDVs) operate at high-voltage and increased temperature, prioritizing reduction in kinetic losses and crossover, and optimization of local catalyst-ionomer interactions within the MEA [3]. The cost dynamics permits higher PGM loadings (~0.3 mg_{Pt} cm^{-2}) compared to LDVs, but long-term durability remains constrained by electrochemically active surface area (ECSA) loss, largely driven by platinum dissolution and redeposition under potential cycling between 0.6 and 0.95 V [3].

The cathodic oxygen reduction reaction (ORR) represents the primary source of performance losses due to its inherently slow kinetics. The catalytic activity is critically dependent on factors such as nanoparticle size, surface topology, electronic characteristics, and the structural properties of the support material [21].

Enhancing ORR activity relies on advanced catalyst architectures [22], typically based on PtM/C alloys (M e.g. Co, Ni, Cu, Fe) [3]. Transition metal alloying introduces lattice contraction and modifies Pt's electronic structure, reducing intermediate binding and increasing active site availability [8]. Transition metal leaching during assembly and operation can be mitigated using catalysts with reduced metal content (e.g., ~10 % Co), achieving uniform nanoparticle distributions, and increasing the initial particle size to around 4–5 nm, thus balancing durability and mass activity [23]. The dominant degradation mechanisms affecting PtM/C catalysts can be further mitigated at the system level through appropriate operating strategies, including optimized voltage windows and load management [23].

The current research is also increasing the focus on carbon support structures, as HDVs require robust catalyst-support combinations that minimize particle mobility, resist ionomer poisoning, and provide strong corrosion resistance [3]. Carbon supports range from highly graphitized, corrosion-resistant types to high-surface-area (HSA) mesoporous carbons, which, though less stable, enhance mass activity and oxygen accessibility [24]. In particular, carbon supports with an optimal internal pore size of 4–7 nm have demonstrated improved ORR activity and transport properties [22].

Research is actively exploring more stable supports, including refractory metal oxides, carbides, nitrides, heteroatoms-doped carbons, and graphitized carbons to enhance durability and catalyst stability [3].

Nitrogen-doped carbons have shown particularly beneficial effects due to the alteration of the electronic structure and surface properties, enhancing Pt anchoring and nanoparticle dispersion [2,25,26]. In particular, nitrogen functional groups—such as pyridinic and pyrrolic moieties—can act as additional heterogeneous nucleation and anchoring sites, promoting uniform Pt coverage, reduced nanoparticle agglomeration, and narrower particle size distributions, especially when Pt nanoparticles are synthesized in-situ on the support surface [25,27]. By combining density functional theory (DFT) simulations with high-angle annular dark-field scanning transmission electron microscopy (HAADF-STEM) and nitrogen elemental mapping, Pylypenko et al. demonstrated that Pt nanoparticles preferentially nucleate in carbon regions neighboring nitrogen-rich areas, rather than directly on nitrogen defects, resulting in stable anchoring and suppressed nanoparticle coalescence [28].

Beyond their role in Pt dispersion, nitrogen-doped supports strongly influence ionomer–support interactions. Coulombic interactions between nitrogen moieties and -SO_3^- groups of ionomer side-chains ensure a more homogeneous ionomer distribution within the catalyst layer [29], without poisoning the catalyst particles [30]. This effect has been quantitatively demonstrated by Ott et al. through CO stripping–derived electrochemical active surface area measurements, which allowed the determination of dry proton accessibility as a direct indicator of ionomer coverage and proximity to Pt nanoparticles. They have shown that N-modified supports display higher dry proton accessibility than Pt/Ketjenblack, where a lower accessibility was attributed to inhomogeneous ionomer distribution rather than to differences in Pt particle location [29].

N-moieties may also change the hydrophobicity and, thus, water management, which is particularly important in controlling relative humidity sensitivity [31]. Martin et al. observed an increased wettability for N-doped carbon relative to Ketjenblack, which they correlated to the enhanced electrochemical performance, as it facilitates effective ionomer distribution and reactant transport under low-humidity conditions [2]. Such advancements have practical implications for PEMFC commercialization, as high dry proton accessibility can significantly reduce system costs by minimizing humidification requirements.

Despite these beneficial effects, the impact of nitrogen doping on ORR activity remains a complex and multifactorial issue. The ORR performance is influenced by a combination of factors, including Pt nanoparticle size and dispersion, support porosity, surface chemistry, wettability, and ionomer distribution, which often change simultaneously upon nitrogen doping [25]. Although DFT and electrochemical studies suggest that nitrogen moieties may facilitate oxygen adsorption and lower energy barriers for O_2 dissociation on Pt surfaces [27], isolating intrinsic electronic effects from concomitant morphological and structural modifications remains challenging. Indeed, several studies indicate that apparent ORR enhancements may arise primarily from changes in pore structure or nanoparticle location, rather than from direct nitrogen-induced electronic effects [29,31].

At the catalyst/ionomer interface, reducing the ionomer side-chain length has demonstrated to improve ECSA and proton transport, increasing PEMFC performance. Short-side-chain perfluorosulfonic acid (SSC-PFSA) ionomers are structurally similar to long-side-chain (LSC) PFSA ionomers like Nafion®, but they feature shorter pendant side-chains with increased crystallinity and elevated thermal transition temperatures [32]. This enables higher ion exchange capacity (IEC) without compromising stability through dissolution or excessive

swelling. SSC ionomers also retain water more effectively within the cathode catalyst layer, improving local proton conductivity and supporting balanced proton and oxygen transport for improved Pt utilization [33–35].

Despite extensive literature on nitrogen-doped carbon supports, catalyst architectures, and short-side-chain ionomers, these innovations have largely been investigated independently, limiting the understanding of their potential combined impact on oxygen transport, proton accessibility, and water management, which are particular relevant under heavy-duty PEMFC operating conditions. The present study aims to address this critical gap in the literature by isolating and rationalizing the individual and combined effects of these promising materials, thereby revealing performance gains often masked in conventional architecture.

This work builds directly on our previous study [36], which showed that the intrinsic advantages of the SSC ionomer Aquivion® D79 cannot be fully exploited when paired with dense, low-porosity carbon supports such as Vulcan/XC72, where the limited pore volume and the lack of mesoporosity hinder water accommodation and removal, causing flooding under fully humidified, high-current-density conditions.

To overcome this limitation, a non-commercial nitrogen-doped mesoporous multifunctional carbon support (MFCS) was employed, and a systematic, stepwise experimental strategy is adopted to first isolate the effect of the support architecture under identical membrane and ionomer conditions and subsequently assess the impact of ionomer chemistry by replacing Nafion® with Aquivion® D79. The combined selection of mesoporous nitrogen-doped carbon, PtCo alloy and SSC ionomer aims to balance kinetic performance and mass transport, enhancing PEMFC operation across a broad range of current densities and ultimately contributing to compact, high-power-density systems for heavy-duty transport.

The present study is intended as a materials-focused and application-oriented investigation, establishing a necessary foundation for subsequent evaluation under elevated temperatures, low-humidity operation, and extended durability protocols representative of heavy-duty systems.

2. Materials and methods

2.1. Materials

This study examined the performances of PEMFCs using two distinct types of catalysts: the commercial Vulcan carbon-supported Pt nanoparticle catalyst (Pt 47 wt% on Vulcan XC72, TEC10V50E, manufactured by Tanaka, referred to as Pt/XC72), and the non-commercial nitrogen-doped carbon-supported PtCo nanoparticle catalyst (PtCo 47 wt% on multifunctional carbon support doped with nitrogen, CORcat-C4-47P, manufactured by pH Matter, referred to as PtCo/MFCS).

The MFCS support, although described as a HSA carbon, differs markedly from conventional HSA carbons such as Ketjenblack. According to the manufacturer, it exhibits a surface area of 650–750 $m^2 g^{-1}$ and a morphology characterized by shallower, more surface-accessible mesopores with lower tortuosity, rather than the deeply interconnected microporous network typically observed in classical HSA carbons [37].

The first comparison between the two catalysts was conducted using Nafion® as ionomer (EW 1100 g mol^{-1}), starting from a dispersion 10 wt % in H_2O from Sigma-Aldrich. Subsequently, the non-commercial catalyst was tested in combination with Aquivion® D79-25BS (25 wt% in H_2O, EW 790 g mol^{-1}, Sigma-Aldrich, referred to as D79).

The membrane used was Nafion® 212, a PFSA membrane with a thickness of 50 μm. The materials employed for the experimental testing are summarized in Table 1.

2.2. Preparation of catalytic ink and MEA

To prepare the catalytic ink, the catalyst and ionomer were first dispersed in a solvent mixture of isopropanol and water. The alcohol-to-water mass ratio was set at 1:1 for Pt/XC72 and increased to 2:1 for PtCo/MFCS, as recommended by the manufacturer. Solvent proportions were adjusted to maintain a solid content of 1 wt%, corresponding to the total mass of catalyst powder and dried ionomer. For Nafion®-based MEAs, an ionomer-to-carbon (I/C) ratio of 0.8 was fixed, as it provides an optimal balance between proton conductivity, gas diffusion, and electrical resistance, as reported in the literature [38]. For D79-based MEAs, the I/C ratio was adjusted to 0.6 to achieve the same amount of sulfonic acid groups per unit carbon mass, facilitating a direct comparison of the two ionomers with different equivalent weights, as described in the study by Ramaswamy et al. [39]. To ensure homogeneity, the ink mixture was initially stirred for 60 min and then sonicated in a temperature-controlled water bath for an additional 30 min.

A commercial GDL with a PTFE-treated microporous layer (Freudenberg H14C9) was used as the gas diffusion medium. The catalytic ink was applied directly onto the GDL's microporous layer at approximately 90 °C using an airbrush. The platinum loading was maintained between 0.20 and 0.30 mg_{Pt} cm^{-2} for both the anode and cathode in order to respect the DOE target for heavy-duty, with actual Pt loading measured by weighing the GDL before and after ink application.

The electrodes were cut to achieve an active area of 4.84 cm^2. The MEA was then prepared by hot pressing the Nafion® membrane between two GDEs and gaskets at 120 °C and 10 bar for 90 s, after which the MEA

Table 1
Materials used for the experimental campaign.

	Material	Supplier	Characteristics
Catalysts	TEC10V50E	Sigma-Aldrich	Pt 47 wt% on Vulcan XC72
	CORcat-C4-47P	Provided by pH Matter	PtCo 47 wt% on MFCS doped with nitrogen
Ionomer	Nafion®	Sigma-Aldrich	10 wt% in H_2O, eq. wt. 1100 g mol^{-1}
	Aquivion® D79	Sigma-Aldrich	25 wt% in H_2O, eq. wt. 790 g mol^{-1}
Membrane	Nafion® 212	Frontis Energy	50 μm Nafion® membrane
Gas Diffusion Layer	Freudenberg H14C9	Quintech	180 μm, with microporous layer

Table 2
Characteristics of tested MEAs. The anode and cathode were fabricated from the same deposition batches, ensuring identical catalyst and ionomer composition and loadings at both electrodes.

Sample	Catalyst	Pt load, mg_{Pt} cm^{-2}	Ionomer	I/C	Membrane
MEA-ref	Pt/XC72	0.33	Nafion®	0.80	Nafion® 212
MEA 1	PtCo/MFCS	0.20	Nafion®	0.80	Nafion® 212
MEA 2	PtCo/MFCS	0.29	D79	0.61	Nafion® 212

was allowed to cool under pressure to prevent mechanical stress. The membranes were used as received. The MEAs prepared for the testing are summarized in Table 2.

2.3. Electrochemical characterization

The performance evaluation of MEAs was conducted utilizing a commercial 5 cm^2 cell hardware from Scribner, which included two graphite end-plates featuring single-serpentine flow fields. The cell was assembled with a torque of 8 N m, using gaskets on both cathode and anode to assure 10 % of MEA compression.

All experiments were carried out with the Scribner 850 Fuel Cell Test System, equipped with an integrated Scribner 885 Potentiostat. The experimental protocol consisted of several steps, including break-in, cyclic voltammetry (CV), hydrogen crossover, H_2/O_2 and H_2/air polarization curves, and H_2/air electrochemical impedance spectroscopy (EIS). After each change of gas, the cell was allowed to stabilize until the open circuit voltage (OCV) reached a steady value, before proceeding with data acquisition. Each step is detailed in the following paragraphs and schematically reported in Table S1 of the supporting information. All in-situ electrochemical tests were performed on two independently prepared MEAs to ensure reproducibility and reliability of the measured results.

2.3.1. Break-in

The break-in procedure was divided into two distinct phases, following the protocol provided by the catalyst manufacturer, pH Matter, to effectively activate the catalyst. The first phase involved a temperature ramp from room temperature to 80 °C under H_2/air conditions at 100% relative humidity (RH). During this phase, the cell was cycled 20 times between 0.6 V for 20 s and 0.1 V for 10 s; a method that also helps to eliminate contaminants at lower potentials. The detailed protocol applied is presented in Table 3.

In the second phase, the cell was held at 0.6 V until the current was stable, which required approximately 30 min. This stabilization phase was conducted at 80 °C, 100 % RH, and a pressure of 2.5 bar absolute.

2.3.2. Cyclic voltammetry

For CV tests, the cell was kept at a temperature of 40 °C and atmospheric pressure. First, a cathode surface cleaning step was performed by conducting a repeated cyclic voltammetry under 200/50 sccm H_2/N_2 with a voltage range of 0.05 V–1.0 V at 500 mV s^{-1} scan rate for 200 cycles. Subsequently, CV measurement was conducted with 100 mV s^{-1} scan rate for 5 cycles, same voltage range and same gas flow rates.

2.3.3. Hydrogen crossover

The hydrogen crossover tests were conducted using 300 sccm of H_2 at the anode and 500 sccm of N_2 at the cathode. For each operating conditions reported in Table 4, a linear sweep voltammogram (LSV) was performed between OCV and 0.6 V with a scan rate of 1 mV s^{-1}. Each measurement was repeated twice to ensure reproducibility.

2.3.4. Electrochemical impedance spectroscopy measurements

The EIS measurements were conducted using 300/500 sccm of pure H_2 on anode and air on cathode, under the same operating conditions as those used for the polarization curves and reported in Table 4. For each operating condition, three different EIS measurements were performed in galvanostatic mode at current densities of 0.1 A cm^{-2}, 0.5 A cm^{-2} and 1.0 A cm^{-2}, in order to study the kinetics, ohmic and transport-limited regions, respectively. Prior to each EIS measurement, the cell was held at the specified current for 5 min to ensure stabilization. The EIS data were collected by applying an amplitude of 5 % DC current over a frequency range from 20 kHz to 0.1 Hz, with a recording rate of 10 points per decade. Each EIS measurement was repeated twice to ensure reproducibility.

Table 4
Operating conditions of the testing procedure for recording polarization curves.

Temperature/°C	Pressure/bar(abs)	Relative humidity/%	
		Anode	Cathode
80	1	100	100
80	2	100	100
80	2	50	50
80	2	33	33

2.3.5. Polarization curves

The H_2/O_2 polarization curve measurement was performed in galvanostatic mode, on the cathodic direction from 0 to 4 A cm^{-2}, with 0.05 A cm^{-2} steps. Each step of the polarization curve was held for 10 s and the measurement was interrupted at a cell voltage of 0.4 V. The anode and cathode flow rates were maintained at 300 and 350 sccm, respectively.

The H_2/air polarization curve measurement was performed in galvanostatic mode, on the cathodic direction from 0 to 3 A cm^{-2}, with 0.05 A cm^{-2} steps. Each step of the polarization curve was held for 10 s and the measurement was interrupted at a cell voltage of 0.4 V. The anode and cathode flow rates were maintained at 300 and 500 sccm, respectively.

During the polarization curve measurement, high frequency resistance (HFR) was measured under the same operating condition using a built-in function of the potentiostat, which performed a single point impedance calculation at 1 kHz.

The operating conditions used for recording the polarization curves are reported in Table 4. During the tests, when adjusting the relative humidity conditions, H_2/N_2 was flowed through the cell for at least 30 min to ensure it reached steady-state under the new operating conditions.

2.4. Structural characterization

2.4.1. X-ray diffraction

A Philips X'Pert PW3040 diffractometer was employed to perform X-ray diffraction (XRD) on the as-received catalyst powders, using Cu Kα radiation ($\lambda = 1.5418 \times 10^{-10}$ m), a 0.013° step size and a 0.2 s $step^{-1}$ acquisition time. The assignation of the diffraction peaks was carried out referring to the Powder Diffraction Files database (International Centre of Diffraction Data).

Table 3
Phase 1 of break-in protocol: temperature ramp while cycling the cell between 0.6V (20s) and 0.1V (10s) for 20 cycles.

	Cell temperature/°C	Gas temperature/°C	Pressure/bar(abs)	Flow rates/sccm	
				Anode (H_2)	Cathode (Air)
Step 1	30	30	1	300	500
Step 2	45	45	2		
Step 3	65	65	2.5		
Step 4	80	80	2.5		

2.4.2. Field emission scanning electron microscopy

Top view images of the CL surface after deposition on GDLs were acquired using a field emission scanning electron microscope (FESEM), specifically a Zeiss Merlin equipped with a Gemini-II column and an Oxford x-act X-ray detector. The instrument was operated at 3 kV in secondary electron mode. Energy Dispersive X-ray Spectroscopy (EDX) mapping was carried out on selected areas of the catalyst layer top view to quantify the ratio between platinum and cobalt in the catalyst. Cross-section images of the different MEAs were also acquired for precise measurement of CL thickness for each type of CL. For the cross-sectional imaging, the instrument was operated at 15 kV in backscattering electron mode to allow a clearer distinction of the CL from the adjacent PEM and GDL layers, since areas containing heavier elements (e.g., Pt) appear brighter compared to polymeric or carbon-based regions. The samples were prepared by immersing the MEAs in liquid nitrogen and then fracturing them to expose the cross-section. Thickness values were calculated by performing multiple measurements at various points on the CL and averaging them to ensure accuracy and account for any potential variability across the layer.

2.4.3. Transmission electron microscopy

Transmission electron microscopy (TEM) analysis was conducted using a TALOS F200X microscope from Thermo Fisher Scientific, operated at an acceleration voltage of 60 kV. High-resolution imaging was achieved using a 16-megapixel CMOS camera (CETA, also from Thermo Fisher Scientific). Images were captured either in high-resolution TEM (HRTEM) configuration or bright field TEM mode, utilizing 30-μm objective aperture. The purpose of TEM analysis was to evaluate the different morphologies and particle sizes of the two catalysts used in this study. For the analysis, the catalyst powders were diluted in isopropanol and thoroughly stirred to create a homogeneous suspension. Drops of this dispersion were deposited onto a carbon-coated copper TEM grid for analysis. To determine the mean particle size of the Pt catalysts, measurements were conducted on TEM images by analysing at least 200 visible particles to ensure statistically significant results.

2.4.4. Dynamic light scattering and zeta potential

Dynamic light scattering (DLS, Zetasizer Nano ZS90, Malvern Instruments, Malvern, Worcestershire, UK) was employed to evaluate the particle size distributions, while ζ-potential measurements were carried out to assess the stability of the different suspensions. The temperature was set at 25 °C, and the scattering angle was 90°. Both the catalyst powders in solvent and the catalytic ink containing catalyst and ionomer were analysed. This approach allowed the evaluation of differences between the two catalysts employed in this work and the influence of ionomers on particle size distribution and colloidal stability of the suspension. The water-to-isopropanol ratio in the solvent was maintained identical to that used in the electrochemical tests, while the samples were diluted 1:1000. For size analyses, 1 mL of the diluted sample was inserted into a capped disposable polystyrene cuvette to prevent solvent evaporation. All measurements were performed in triplicate.

2.4.5. N_2 physisorption

N_2 physisorption experiments were conducted at 77 K using a Micromeritics ASAP 2020 analyser. Both catalysts and CLs were analysed in their powder form, with each sample weighing approximately 90 mg. Prior to the adsorption experiments, the pristine catalysts were degassed at 150 °C for 2 h, while the catalytic ink – prepared following the same procedure used for electrochemical tests – was dried overnight at 60 °C, placed in the sample holder, and degassed at 115 °C for 3 h. Adsorption measurements were performed immediately after degassing.

Adsorption isotherms for both catalysts and catalytic layers were normalized to the carbon content of each sample. The Brunauer-Emmett-Teller (BET) method was used to determine the specific surface area (BET SA_{total}), considering a range of 0.05–0.3 P/P_0. The total pore volume ($V_{pore,\ total}$) was estimated at a relative pressure of 0.98 P/P_0 in standard conditions and converted using a conversion factor of 0.001547, assuming that the density of condensed N_2 within the pores is equivalent to that of bulk liquid N_2 [40].

Pore-size distributions were determined using the Barrett-Joyner-Halenda (BJH) method, considering the desorption branch of the isotherms [40].

The t-plot method was used to calculate the micropore volume ($V_{pore,\ <2nm}$) and the external and mesopore surface area ($SA_{>2nm}$). The thickness of the adsorbed layer on the pore wall t (Å) was computed as function of P/P_0, according to Harkins-Jura equation [40], and the isotherms were replotted as function of t:

$$t = \left(\frac{13.99}{0.034 - log\left(\frac{P}{P_0}\right)} \right)^{1/2} \quad (1)$$

The linear region of the isotherms between 5 and 15 Å was interpolated, obtaining $SA_{>2nm}$ and $V_{pore,\ <2nm}$ from the slope and intercept, respectively.

2.4.6. X-ray photoelectron spectroscopy

X-ray photoelectron spectroscopy (XPS) measurements were performed on Pt/XC72 and PtCo/MFCS as-received catalyst powders, as well as on catalyst layers containing both catalyst and ionomer, in order to assess surface composition, platinum electronic state, ionomer coverage, and metal–ionomer interactions. Catalyst layer samples were prepared by cutting small pieces of sprayed electrodes and analysed as intact layers. The surface composition of the different samples was investigated by XPS using a PHI 5000 VersaProbe instrument. Survey spectra were acquired with a pass energy of 187.85 eV, a take-off angle of 45°, and an X-ray spot diameter of 100 μm, while high-resolution (HR) spectra of C 1s and Pt 4f were collected using a pass energy of 23.50 eV. All spectra were referenced to the C 1s core level at 284.5 eV [41] to compensate for surface charging effects. Data analysis was performed using CasaXPS software.

3. Results and discussion

3.1. Ex-situ characterization

3.1.1. Morphology and porosity of the catalyst layers

To investigate the crystalline structure of the catalysts, XRD analysis was carried out. The corresponding diffraction patterns are shown in Fig. 1, which compares the structural features of the commercial Pt/XC72 catalyst and the PtCo/MFCS material.

The XRD pattern of Pt/XC72 displays the characteristic diffraction peaks of face-centered cubic (fcc) platinum, with intense reflections at approximately 39.8°, 46.2°, and 67.5°, corresponding to the (111), (200), and (220) planes, respectively (JCPDS, reference number 01-087-0640). These peaks confirm the presence of crystalline metallic Pt nanoparticles supported on Vulcan carbon.

In contrast, the PtCo/MFCS catalyst exhibits diffraction peaks slightly shifted toward higher diffraction angles compared to pure Pt due to the presence of Co. This shift is attributed to the incorporation of Co atoms into the Pt lattice. Since Co has a smaller atomic radius than Pt, its substitution leads to a lattice contraction, thereby decreasing the average unit cell dimensions. This phenomenon is consistent with previous literature reports on structurally ordered PtCo-based catalysts [42]. The diffraction peaks of PtCo/MFCS also exhibit smaller widths compared to those of Pt/XC72. According to the Scherrer equation, this difference is associated with larger average crystallite sizes for the PtCo alloy particles (5.5 nm) with respect to the Pt/XC72 ones (3.5 nm), which may result from the alloying process.

Fig. 2 shows the FESEM images of the top view of the different samples. The images clearly reveal significant differences between the

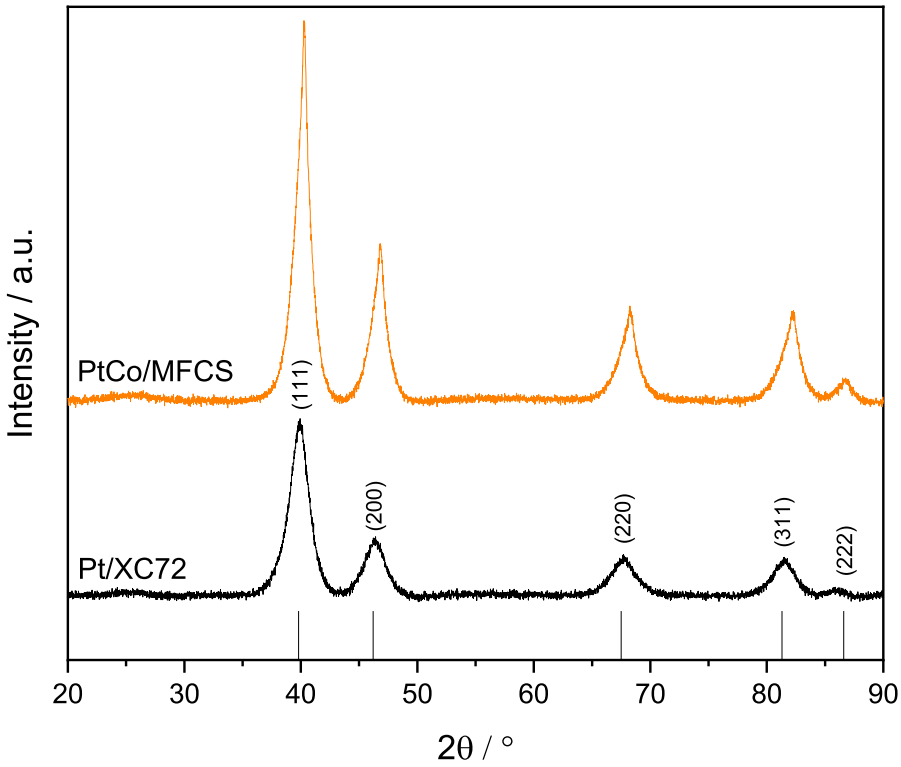

Fig. 1. XRD patterns of Pt/XC72 and PtCo/MFCS catalysts.

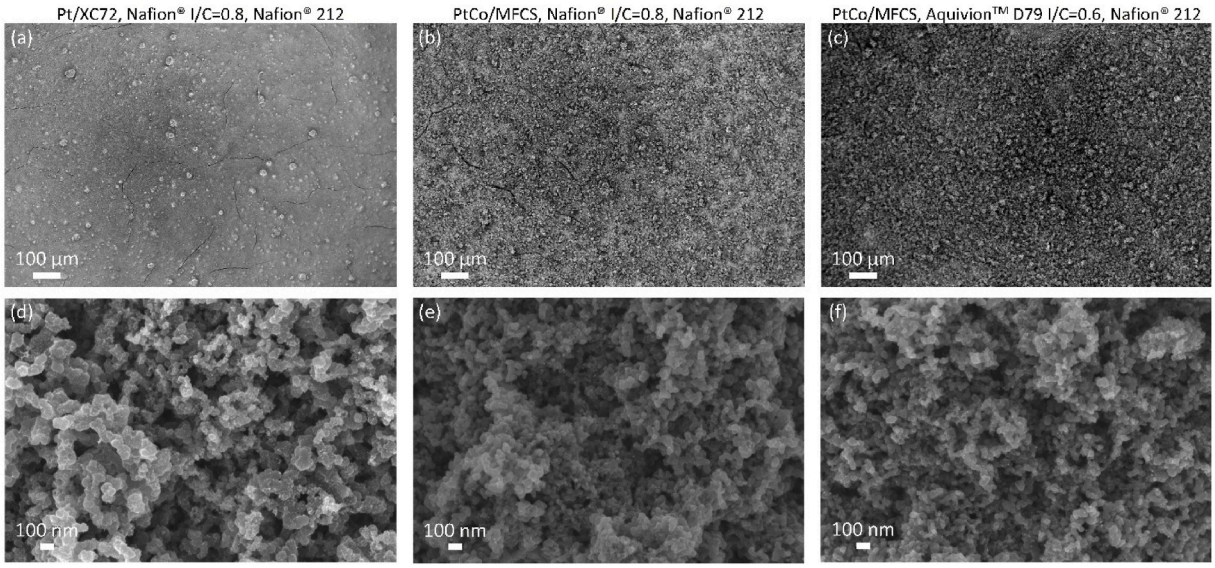

Fig. 2. FESEM images representing electrode top view of (a, d) Pt/XC72 (0.3 mg_{Pt} cm^{-2}) with Nafion® ionomer (I/C 0.8) , (b, e) PtCo/MFCS (0.2 mg_{Pt} cm^{-2}) with Nafion® ionomer (I/C 0.8), (c, f) PtCo/MFCS (0.3 mg_{Pt} cm^{-2}) with D79 ionomer (I/C 0.6).

Pt/XC72-based electrodes and those based on PtCo/MFCS. The surface of the PtCo/MFCS-based electrodes, shown in Fig. 2(b) and (c), presents a higher roughness, in contrast to the smoother surface of the Pt/XC72 electrodes in Fig. 2(a). Additionally, the Pt/XC72-based sample shows a higher degree of cracking, which appears to be reduced in the PtCo/MFCS electrodes, particularly when D79 is used as the ionomer (Fig. 2 (c)). Furthermore, the higher magnification FESEM images reported in Fig. 2(d–f) allow a more detailed comparison of the catalyst layer morphology. In particular, the Pt/XC72 electrode (Fig. 2(d)) shows larger carbon support particles compared to the PtCo/MFCS-based samples (Fig. 2(e and f)), indicating a lower degree of dispersion of the catalytic phase. The PtCo/MFCS electrodes, by contrast, display smaller carbon domains and a more finely structured catalyst layer, which is expected to contribute to an increased ECSA. In addition, the D79-based electrode (Fig. 2(f)) appears less agglomerated than the Nafion®-based counterpart (Fig. 2(e)), suggesting a more open morphology with improved porosity of the ionomer/catalyst layer.

Cross-sectional FESEM images (Fig. S1) further confirm the

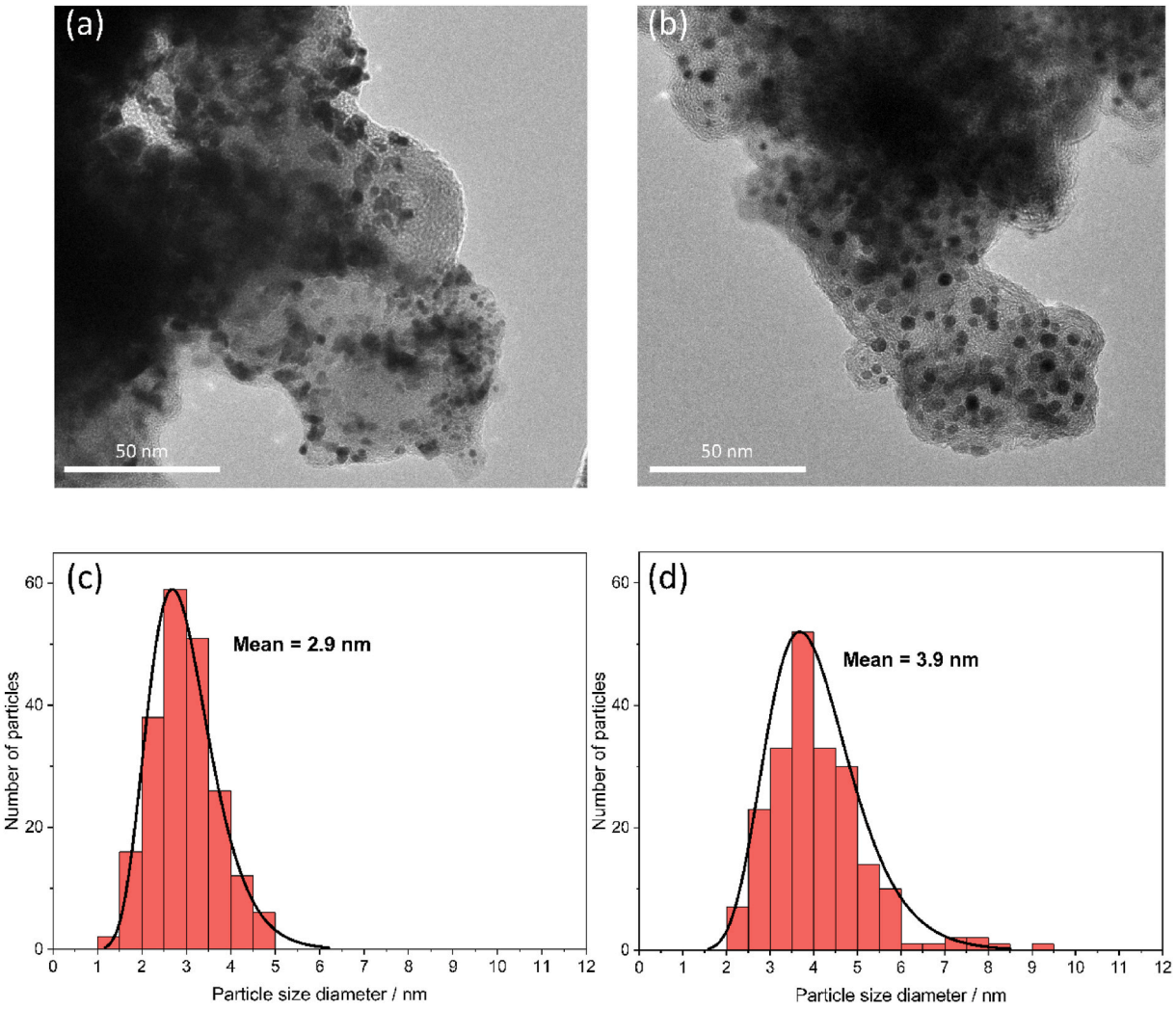

Fig. 3. TEM images and particle size distribution of (a,c) Pt/XC72, and (b,d) PtCo/MFCS.

morphological differences between the two catalysts. In particular, the Pt/XC72-based CL exhibits a relatively flat and compact profile, whereas the PtCo/MFCS layer shows a markedly rougher and more textured morphology. This increased roughness is expected to influence the interfacial resistance with the membrane, potentially affecting cell performance. In addition, the cross-sections highlight the different film thicknesses, which align well with the respective catalyst loadings.

The elemental analysis conducted with EDX mapping (Fig. S2 and Table S2) revealed that the Co/Pt atomic ratio in the catalyst was 10.6 %.

TEM analysis was conducted to investigate the morphological characteristics and particle size distribution of Pt/XC72 and PtCo/MFCS. Fig. 3 provides representative TEM images, highlighting the distinctive features of the catalysts. The TEM images reveal significant differences in particle size and distribution between the catalysts. As reported in Fig. 3(a) and (b), Pt/XC72 exhibits smaller particles compared to PtCo/MFCS. However, these smaller particles tend to form aggregates on the support material, leading to a less uniform spatial distribution. This aggregation may influence the accessibility of active sites and, consequently, the overall electrochemical performance of the MEA. In contrast, PtCo/MFCS catalyst shows a notably more uniform distribution of the catalyst particles on the support. This uniformity can be associated with nitrogen doping of the carbon support, which introduces functional groups or defects into the carbon matrix that serve as nucleation sites for metal particles, preventing aggregation and promoting uniform dispersion. The particle size distribution analysis from TEM images (Fig. 3c and d) confirms that PtCo/MFCS consists of larger particles than Pt/XC72. Specifically, Pt/XC72 exhibits an average particle size of 2.9 nm, compared to 3.9 nm observed for the PtCo/MFCS. Although the absolute values obtained by TEM and XRD differ slightly,

Table 5
Microstructural characteristics of catalysts and catalytic layers powders determined from N_2 adsorption isotherms.

	BET $SA_{total}/m^2\ g^{-1}_{carbon}$	$SA_{>2nm}/m^2\ g^{-1}_{carbon}$	$SA_{<2nm}/m^2\ g^{-1}_{carbon}$	$V_{pore,\ total}/cm^3\ g^{-1}_{carbon}$	$V_{pore,\ <2nm}/cm^3\ g^{-1}_{carbon}$
Pt/XC72	188 ± 4	112 ± 3	77 ± 5	0.338	0.038 ± 0.003
Pt/XC72 + Nafion	155 ± 3	89 ± 3	66 ± 4	0.325	0.031 ± 0.003
PtCo/MFCS	669 ± 8	356 ± 5	312 ± 9	1.043	0.169 ± 0.005
PtCo/MFCS + Nafion	514 ± 5	276 ± 4	238 ± 7	0.806	0.123 ± 0.004
PtCo/MFCS + D79	523 ± 5	268 ± 4	255 ± 6	0.979	0.132 ± 0.003

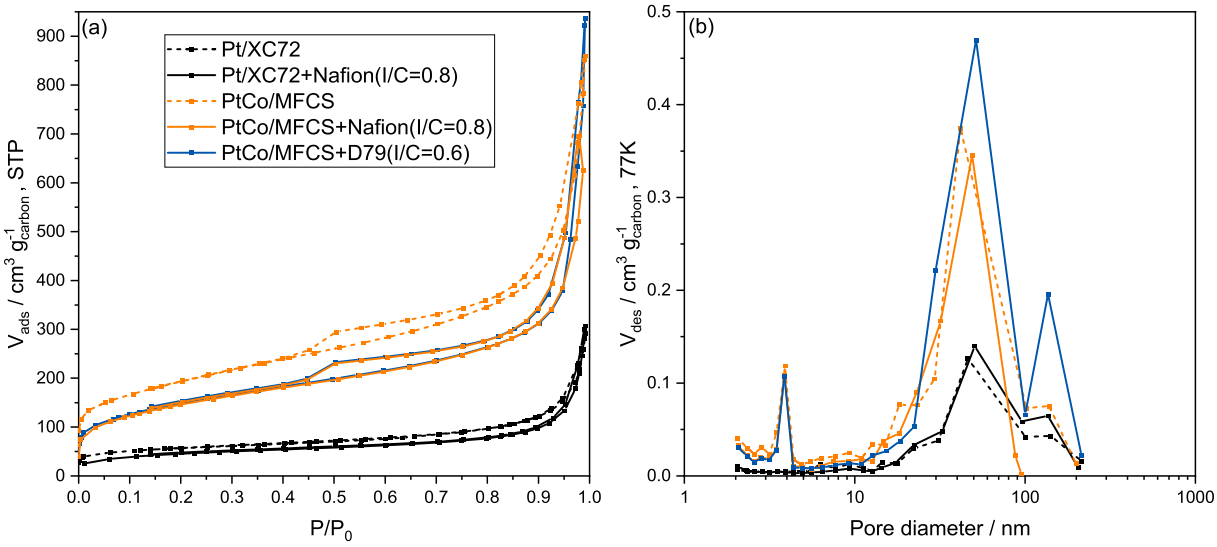

Fig. 4. (a) N_2 adsorption isotherms and (b) pore-size distributions for Pt/XC72 and PtCo/MFCS catalyst powders (dashed lines), and for Pt/XC72 + Nafion®, PtCo/MFCS + Nafion® and PtCo/MFCS + D79 catalytic layer powders (solid lines).

this small discrepancy is expected because the two techniques probe distinct structural features: XRD provides a bulk-averaged crystallite size, whereas TEM resolves individual nanoparticles within a restricted field of view.

Nitrogen physisorption was conducted to compare the surface area and porosity of the pristine catalysts and the CLs with various catalyst-ionomer combinations, evaluating both the difference between the catalysts and the effect of ionomer introduction. The results are reported in Table 5. As expected, Pt/XC72 exhibits a significantly lower total surface area (188 $m^2\ g_{carbon}^{-1}$) compared to PtCo/MFCS (668 $m^2\ g_{carbon}^{-1}$). This difference is attributed to the distinct carbonaceous supports used, as the PtCo/MFCS catalyst is based on high-surface-area carbon while Pt/XC72 is based on Vulcan carbon. The isotherm shapes for the pristine catalyst samples in Fig. 4 further corroborate the relatively smoother and less porous nature of Pt/XC72 compared to the more porous PtCo/MFCS, as previously discussed with respect to the FESEM images. The type IV isotherm illustrates the more predominantly mesoporous character of PtCo/MFCS compared to Pt/XC72, where only a small hysteresis is found. Despite this, the pore-size distribution in Fig. 4(b) shows a pronounced peak around ~50 nm for all samples. Although this feature lies in the macropore range, it is typically attributed to secondary (interparticle) porosity arising from the packing of carbon aggregates. These macropores tend to dominate the cumulative pore volume in carbon-black-based materials due to their inherently larger geometrical contribution [40]. When adding the ionomer, the BET is reduced by about 18 % for Pt/XC72 and by 22–23 % for PtCo/MFCS. As shown in Fig. 4(a), the shape of the isotherms remains unchanged after ionomer addition, shifting downward without altering their overall profile. This indicates that the ionomer forms a thin film that fills the pores without significantly affecting the aggregation or agglomeration characteristics of the carbon support [40]. Furthermore, the pore size distribution graphs in Fig. 4(b) confirm that the ionomers predominantly occupy the micro- and mesopores in a nearly uniform manner, creating a thin film without significantly affecting the pore volume. The only noticeable differences in porosity are observed for pores larger than 40 nm, which corresponds to secondary pores predominantly located in the outer regions and attributed to networks formed between particles due to ionomer distribution. The network formed by D79 (blue solid line in Fig. 4 (b)) is particularly prominent compared to the Nafion®-based sample (orange solid line in Fig. 4(b)), whose trend closely resembles that of the pristine catalyst (orange dashed line in Fig. 4(b)). This observation is particularly relevant for MEA performance, as the proportion of primary and secondary pores affects both gas transport and water management within the catalyst layer. As demonstrated before in literature, an optimal balance ensures that oxygen can diffuse efficiently while water generated during the reaction is adequately retained and distributed, maximizing electrochemical performance at the MEA level [43].

Table 6
Mean diameter size, polydispersion index (PDI) and ζ-potential for the different catalytic dispersions.

	Mean diameter size/nm	PDI/-	ζ-potential/mV
Pt/XC72	204 ± 9	0.21 ± 0.05	−19 ± 6
PtCo/MFCS	209 ± 9	0.23 ± 0.02	−10 ± 1
Pt/XC72 + Nafion	193 ± 12	0.25 ± 0.04	−53 ± 3
PtCo/MFCS + Nafion	199 ± 11	0.28 ± 0.06	−36 ± 6
PtCo/MFCS + D79	206 ± 12	0.30 ± 0.07	−32 ± 2

The different catalysts and ionomers influence the dimensional distribution and structure of the catalyst/ionomer aggregates during ink preparation and after deposition. To further investigate these effects, DLS analysis was conducted on the catalytic inks prepared using various catalysts and ionomers. First, this analysis aimed to compare the size distribution of catalyst aggregates in inks containing Pt/XC72 and PtCo/MFCS catalysts, independently of the effect of the ionomer. This approach was necessary because, in addition to having different physicochemical characteristics, ink preparation involved different mass ratios of isopropanol to water depending on the catalyst used. Specifically, for the Pt/XC72 catalyst, the alcohol-to-water mass ratio was set at 1:1, whereas it was increased to 2:1 for PtCo/MFCS. The results of the analysis are reported in Table 6. The similar average diameters observed for both catalysts indicate that the isopropanol-to-water ratio used for PtCo/MFCS shows comparable dispersibility of aggregates, as confirmed in Fig. S3. As also shown in Fig. S3, the addition of different ionomers does not seem to affect the size distribution of the catalyst-ionomer aggregates. The aggregate sizes after ionomer addition are very similar, with the polydispersity indexes also showing comparable values, as reported in Table 6. Therefore, the analysis suggests that the type of ionomer does not influence the aggregates size. However, this result could be closely related to the limitations of the instrument, as it requires an extremely high dilution (1:1000) compared to real conditions, where the particles, being much closer, could interact differently. Under those conditions, the type of ionomer and catalyst could indeed influence the size and distribution of the aggregates.

Table 7
Quantitative XPS analysis of the C 1s and Pt 4f core-level spectra for pristine catalysts (Pt/XC72 and PtCo/MFCS) and the corresponding catalyst layers after ionomer incorporation (Pt/XC72 + Nafion®, PtCo/MFCS + Nafion®, and PtCo/MFCS + D79). Values are reported as relative atomic concentrations (%Conc) obtained from peak deconvolution, expressed in compact form and normalized to the total C 1s or Pt 4f envelope.

	Pt/XC72	Pt/XC72 + Nafion®	PtCo/MFCS	PtCo/MFCS + Nafion®	PtCo/MFCS + D79
sp^2 C–C/C=C	53.39	39.75	51.37	37.90	41.02
sp^3 C–C	30.59	11.19	27.21	27.71	25.80
C–O/C=O[a]	6.58	9.52	7.52	6.38	5.27
O–C=O/COOH[a]	9.45	13.17	13.91	7.06	4.14
$C–F_2$/O–CF_2	–	16.15	–	16.88	23.78
$C–F_3$	–	10.21	–	4.08	–
Pt^0	38.16	31.74	49.67	42.39	32.66
Pt^{2+}	33.22	47.11	40.66	36.48	47.94
Pt^{4+}	28.61	21.15	9.68	21.13	19.4

[a] Note: The C–O/C=O and O–C=O/COOH components may include overlapping contributions from nitrogen-containing functionalities (e.g., C–N, C=N, N–C=O), particularly for the N-doped MFCS support, due to their similar binding energies in the C 1s region.

However, the higher alcohol content in the PtCo/MFCS formulation may contribute to reduced ink stability. To investigate this, ζ-potential measurements were performed on inks containing only the catalyst and on those with both the catalyst and ionomer. High absolute values of ζ-potential indicate an elevated surface charge, which enhances electrostatic repulsion among the particles, thereby reducing the tendency towards particle aggregation [44]. The results in Table 6 show that inks containing only the catalyst exhibit lower stability, as indicated by lower ζ-potential values. In contrast, the addition of ionomer significantly enhances the stability of the catalytic inks, likely due to the stabilizing effect of the ionomer, which creates a charged layer over the particles helping to prevent particle aggregation.

3.1.2. *Surface chemistry and electronic structure*

To elucidate the intrinsic differences between the two investigated catalysts and to isolate the specific role of the ionomer chemistry, XPS analyses were systematically performed both on the pristine catalyst powders and on the surfaces of the corresponding catalyst layers.

The quantitative results obtained from the deconvolution of the C 1s and Pt 4f core-level spectra are summarized in Table 7. The elemental atomic percentages derived from survey spectra are listed in Table S3, while the deconvoluted C 1s and Pt 4f spectra are shown in Figs. S4 and S5, respectively.

C 1s and Pt 4f spectra were deconvoluted following well-established literature assignments [2,41], with resulting peak assignments reported in Table S4. N 1s spectra were not analysed due to its very low atomic concentration, which prevented reliable peak fitting.

First, the direct comparison between Pt/XC72 and PtCo/MFCS as-received powders highlights marked differences in platinum surface accessibility, Pt electronic state, and support chemistry. The results of XPS survey spectra (Table S3) indicate a substantially higher Pt atomic fraction for Pt/XC72 (≈18.0 at.%) compared to PtCo/MFCS (≈3.3 at.%). Combined with N_2 physisorption results, this difference is attributed to the higher specific surface area and hierarchical porosity of MFCS, which promote deep pore confinement of PtCo nanoparticles beyond the effective XPS probing depth. Accordingly, the attenuated Pt signal for PtCo/MFCS reflects limited XPS accessibility rather than differences in Pt loading (~50 wt% for both catalysts), or a lower intrinsic density of active sites.

Beyond morphological considerations, clear differences also emerge in the surface oxidation state of platinum. Quantitative analysis of the Pt 4f spectra (Table 7) shows a higher fraction of metallic Pt^0 (≈50 %) for PtCo/MFCS compared to Pt/XC72 (≈44 %). This result suggests that the combined effects of Co alloying and nitrogen functionalities contribute to an electronic stabilization of Pt, likely through electron donation from Co and strengthened metal–support interactions induced by N-doping [8,27].

Analysis of the C 1s spectra further highlights distinctions in the chemical nature of the two carbon supports. As expected, PtCo/MFCS catalyst displays a higher fraction of oxidized and functionalized carbon species. The partial overlap of oxygen- and nitrogen-related components within the C 1s envelope, also reported in literature [2], implies that the increased C=O/COOH contribution arises from an intrinsically more defect-rich surface rather than solely from oxygenated functionalities. This assignment is supported by the detectable N 1s signal (~0.9 at.%), as reported in the survey in Table S3, confirming the presence of surface nitrogen species. These surface characteristics are particularly relevant from a functional perspective. Despite maintaining a degree of graphitization comparable to that of Vulcan XC72, as evidenced by the similar fraction of sp^2, the MFCS support combines a higher density of surface functional groups and defects with extensive porosity. Such features are expected to enhance Pt nanoparticle anchoring, strengthen metal–support interactions, improve ionomer–support affinity, and increase surface hydrophilicity, while maintaining an ordered structure with potential improved durability [25]. Collectively, these properties are particularly relevant for heavy-duty applications, which demand operation under harsh conditions, including low humidity and extended durability requirements.

Overall, whereas Pt/XC72 exhibits higher apparent Pt exposure, PtCo/MFCS provides a more electronically stabilized and chemically active environment for Pt, mediated by Co alloying and N-doped functionalities. These intrinsic differences are expected to influence catalytic behavior and interfacial interactions upon MEA integration and constitute a critical framework for interpreting the effects of ionomer addition and the resulting electrochemical performance.

The effect of Nafion® ionomer addition was further investigated by comparing Pt/XC72-based and PtCo/MFCS-based catalyst layers. Survey spectra, reported in Table S3, show comparable fluorine atomic percentages (≈34 at.%) for both systems. When analysing C 1s spectrum, upon ionomer incorporation, both catalysts exhibit a similar trend in sp^2 carbon fraction decrease, as shown in Table 7, indicating a comparable overall degree of carbon surface coverage. However, despite this similar extent of coverage, the evolution of functionalized carbon-related fractions differs significantly, pointing to distinct ionomer–support interaction mechanisms.

For Pt/XC72, Nafion® addition is accompanied by an apparent increase in oxidized carbon-related species in the C 1s spectrum with the combined C=O and COOH components increasing from 16.03% to 22.69%. This increase is interpreted as a consequence of spectral overlap between Nafion®-derived C–O and O–C=O contributions and native carbon functionalities within the 286–289 eV binding energy region. Concomitantly, the Pt 4f spectra show an increased fraction of oxidized platinum species upon ionomer incorporation, indicating a direct interaction between Nafion® and Pt nanoparticles. Taken together, the simultaneous evolution of the C 1s and Pt 4f regions suggests that the observed changes primarily originate from ionomer–platinum interactions, rather than from chemical modification of the carbon support.

In contrast, PtCo/MFCS exhibits the opposite trend upon Nafion® incorporation, with the overall contribution of oxidized carbon-related components in the C 1s spectrum decreasing from 21.43% to 13.44%. This behavior reflects a stronger and more chemically specific involvement of MFCS surface functionalities in ionomer–support interactions. In MFCS, the functionalized carbon region of the C 1s spectrum encompasses overlapping contributions from oxygen- and nitrogen-containing groups, as well as defect-associated sites, which are largely absent in XC72. Interaction with Nafion® alters the local electronic environment of these chemically active sites, leading to an apparent reduction in oxidized carbon-related contributions. Accordingly, this decrease does not indicate a loss of surface functionalities, but rather their effective participation in ionomer anchoring and interfacial interactions, promoting a more homogeneous ionomer distribution. This interpretation is further supported by the lower fraction of oxidized platinum species observed in the Pt 4f spectra compared to Pt/XC72-based catalyst layer, indicating that in PtCo/MFCS the ionomer preferentially interacts with functionalized carbon sites rather than with platinum nanoparticles.

Taken together, the correlated evolution of carbon functional groups and Pt oxidation state demonstrates that the differences observed between Pt/XC72 and PtCo/MFCS-based electrodes originate from fundamentally distinct Nafion®–support interaction modes. These support-dependent interactions govern ionomer distribution, Pt accessibility, and Pt chemical stability, and therefore provide a key framework for interpreting the contrasting electrochemical responses of the corresponding MEAs.

A further level of insight was obtained by directly comparing Nafion® and D79 ionomers on the PtCo/MFCS catalyst. As expected, survey spectra results in Table S3 show a lower fluorine atomic percentage for the D79-based catalyst layer compared to Nafion®-based one, due to its short-side-chain architecture, which contains fewer fluorinated functionalities, as well as to the lower I/C ratio used for its preparation. Moreover, Pt 4f deconvolution reveals a higher degree of Pt oxidation in the presence of D79, which can be attributed to its architecture, characterized by shorter and more flexible side chains that facilitate closer approach and stronger interaction of $-SO_3^-$ groups with the Pt surface.

The analysis of the C 1s region further supports a distinct interaction mode of D79 and Nafion® with the N-doped MFCS support. In the D79-based electrode, the coexistence of a high local C–F contribution and a lower overall fluorine content suggests that D79 forms localized, strongly bound ionomer domains consistent with its SSC architecture, which favor stronger, more localized interactions with polar or defect-rich regions of the carbon support.

Overall, the comparison between Nafion® and D79 on MFCS demonstrates that ionomer chemistry, beyond ionomer loading, plays a decisive role in controlling both the chemical and spatial interactions within the catalyst layer. The distinct interaction modes are expected to critically influence the formation and effectiveness of the triple-phase boundary and provide a rational framework for interpreting the differences in electrochemical performance discussed in the following sections.

3.2. Electrochemical performance

3.2.1. Catalysts comparison

The first part of this study focuses on the assessment of a non-commercial catalyst, PtCo/MFCS, provided by pH Matter, in comparison to a commercial catalyst, Pt/XC72, typically used for these applications. Hence, two MEAs were prepared: one incorporating PtCo/MFCS catalyst and the other employing the commercial Pt/XC72 benchmark catalyst. All remaining MEA constituents (i.e., ionomer and membrane) were held constant (Nafion® ionomer and Nafion® 212 membrane). This controlled configuration ensures that the performance differences can be unambiguously ascribed to the intrinsic properties of the catalyst materials.

The ECSA was determined using cyclic voltammetry, as shown in Fig. S6, by integrating the hydrogen desorption peak and assuming a monolayer charge of 210 μC cm^{-2}. Results indicate that PtCo/MFCS exhibits a larger ECSA, reaching 54 m^2 g_{Pt}^{-1}, compared to 48 m^2 g_{Pt}^{-1} for Pt/XC72. This can be attributed to the superior Pt dispersion on the high-surface-area carbonaceous support of PtCo/MFCS, in contrast to the less efficient Pt dispersion on the lower-surface-area carbon support of Pt/XC72. This trend agrees with TEM and N_2 physisorption analyses and is further supported by XPS results, which reveal a higher density of surface functional groups and nitrogen-related sites on MFCS, together with a higher fraction of metallic Pt. These features indicate stronger metal–support interactions and a more stabilized Pt surface environment. At the same time, XPS evidence of a more distributed ionomer arrangement on MFCS suggests improved ionomer–support affinity without excessive surface blocking. Collectively, the combined effects of

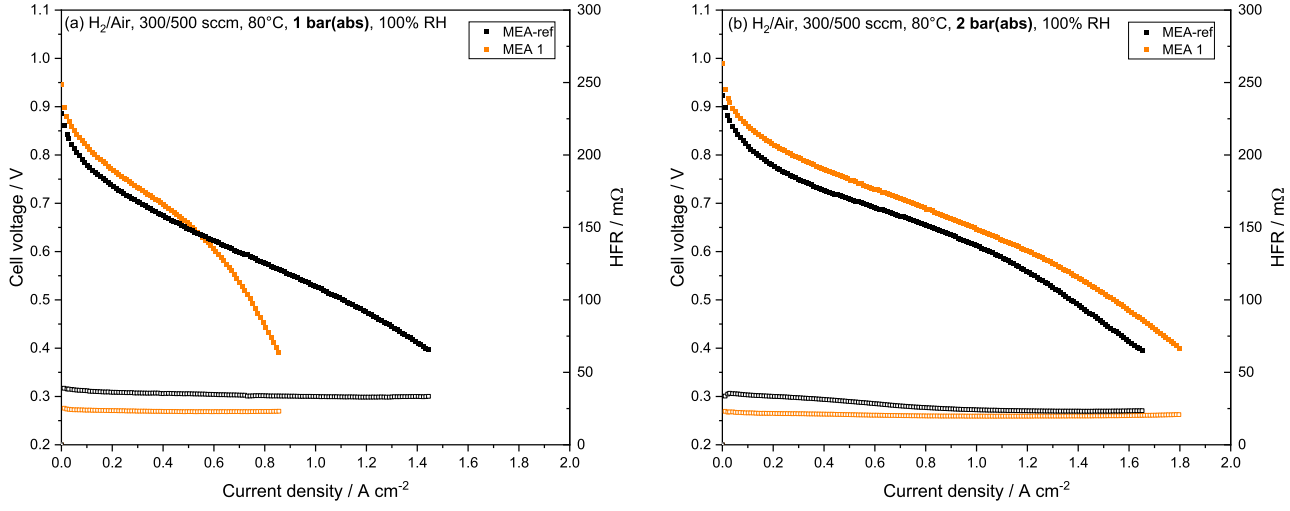

Fig. 5. Polarization curves recorded in H_2/air (300/500 sccm), at 80 °C and RH 100% under (a) 1 bar absolute and (b) 2 bar absolute. The high-frequency resistance (HFR) is indicated on the right y-axis. MEA-ref (black line): Pt/XC72 (0.3 mg_{Pt} cm^{-2}), Nafion® ionomer (I/C 0.8), Nafion® 212. MEA 1 (orange line): PtCo/MFCS (0.2 mg_{Pt} cm^{-2}), Nafion® ionomer (I/C 0.8), Nafion® 212. (For interpretation of the references to colour in this figure legend, the reader is referred to the Web version of this article.)

Co alloying, nitrogen doping, and tailored surface chemistry promote improved Pt anchoring, higher active-site accessibility, and more uniform catalyst-layer nanostructure, thereby facilitating electrochemical reactions and supporting the higher ECSA observed for PtCo/MFCS.

Furthermore, to better understand the differences in terms of performance, the specific mass activity was also measured at 0.9 V vs. RHE under 2 bar absolute and H_2/O_2 conditions, and corrected for iR losses and gas crossover. Values of 32 mA cm^{-2} and 537 mA cm^{-2} were obtained for Pt/XC72 and PtCo/MFCS, respectively. PtCo/MFCS exhibited a more than 16-fold increase in mass activity, demonstrating its superior catalytic performance. This remarkable difference stems from the synergistic effects of the alloying with cobalt and the nitrogen-doped high-surface-area carbon support, which collectively enhance the intrinsic activity of the catalyst and maximize the utilization of platinum.

Fig. 5 (a) and (b) show the polarization curves measured in air at 100% RH and 80 °C, under ambient pressure and at 2 bar absolute, respectively. At ambient pressure, the commercial catalyst Pt/XC72 exhibits better performance compared to the non-commercial PtCo/MFCS catalyst. This behaviour is consistent with the lower platinum surface accessibility typically observed for PtCo catalysts supported on high–surface-area carbons compared to Vulcan XC72, as also reported in the literature [24], and with the reduced accessible Pt fraction for PtCo/MFCS catalyst explained above by XPS results. The performance gap can thus be rationalized by considering mass-transport limitations within the highly porous PtCo/MFCS, where gas diffusion in the nanoscale pore network is expected to be partially governed by Knudsen diffusion. Under low-pressure conditions, the reduced gas density amplifies Knudsen-related transport resistance, limiting oxygen accessibility to internal catalytic sites. In contrast, Pt nanoparticles in Pt/XC72 are predominantly exposed on the external carbon surface, making this catalyst less sensitive to pressure-induced transport limitations. However, the performance trend reverses at 2 bar absolute, where PtCo/MFCS outperforms Pt/XC72. This pressure-dependent behaviour arises from a combination of factors. First, the carbon support in PtCo/MFCS, with its high surface area and optimized porosity, facilitates gas diffusion and reactant transport more efficiently as pressure increases. In this regime, the transport mechanism progressively shifts toward molecular diffusion, improving oxygen availability throughout the porous catalyst layer and enabling a more effective utilization of the high active-site density of PtCo/MFCS. Conversely, the intrinsic higher platinum exposure of Pt/XC72 limits its ability to take advantage of higher operating pressures. In addition, the superior performance of PtCo/MFCS at elevated pressure may also be related to the intrinsic structure of the alloy catalyst [45], particularly the higher roughness evidenced by FESEM (Fig. 2) and the different support morphology observed by TEM (Fig. 3). The increased ECSA and the related higher roughness of PtCo nanoparticles can promote higher turnover frequency as back pressure rises, an effect not observed for pure Pt catalysts.

It is also worth noting that this superior performance of PtCo/MFCS is achieved even though its platinum loading is approximately 43%

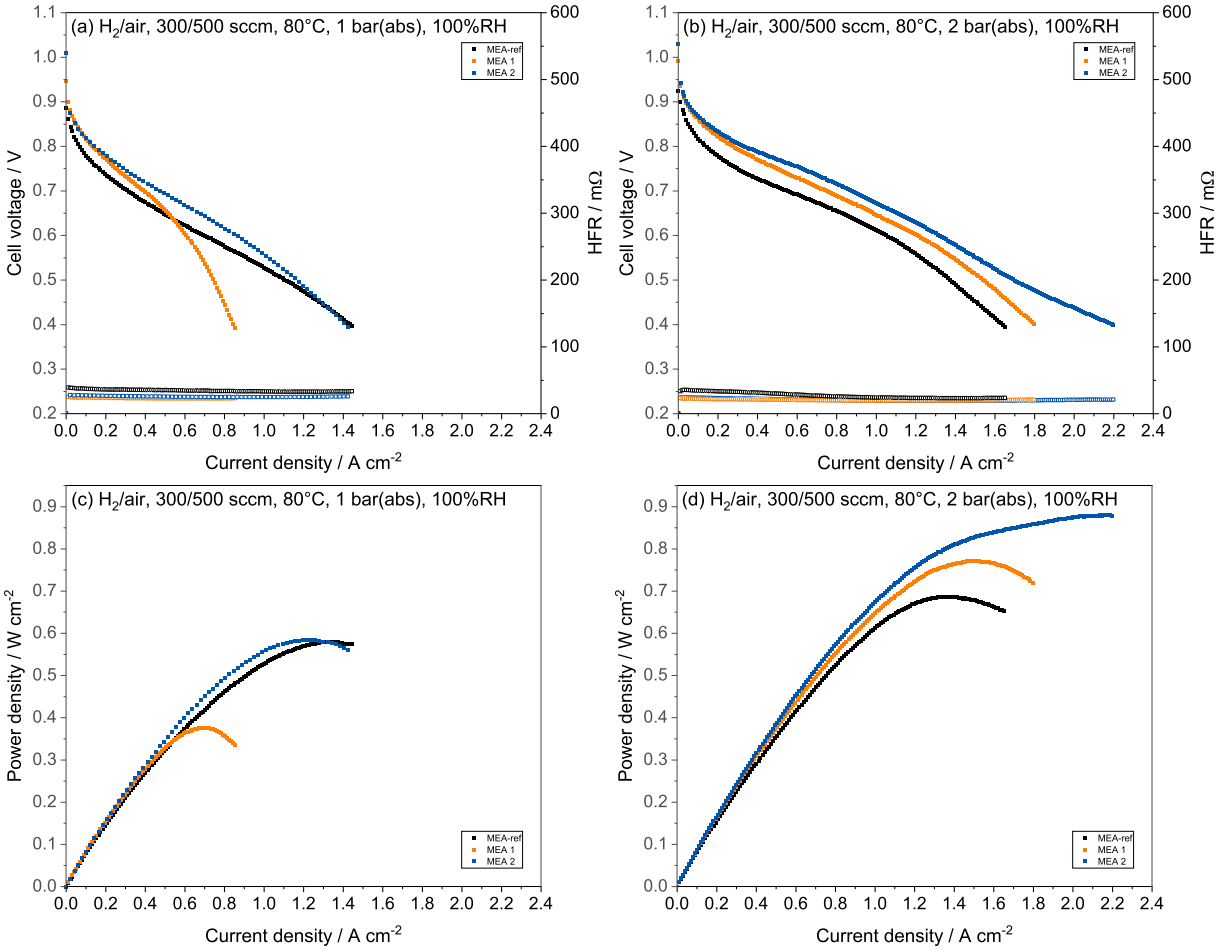

Fig. 6. Polarization curves recorded in H_2/air (300/500 sccm), at 80 °C and RH 100% under (a) 1 bar absolute and (b) 2 bar absolute. The high-frequency resistance (HFR) is indicated on the right y-axis. Power curves recorded in H_2/air (300/500 sccm), at 80 °C and RH 100% under (c) 1 bar absolute and (d) 2 bar absolute. MEA-ref (black line): Pt/XC72 (0.3 mg_{Pt} cm^{-2}), Nafion® ionomer (I/C 0.8), Nafion® 212. MEA 1 (orange line): PtCo/MFCS (0.2 mg_{Pt} cm^{-2}), Nafion® ionomer (I/C 0.8), Nafion® 212. MEA 2 (blue line): PtCo/MFCS (0.3 mg_{Pt} cm^{-2}), D79 ionomer (I/C 0.6), Nafion® 212. (For interpretation of the references to colour in this figure legend, the reader is referred to the Web version of this article.)

lower than that of Pt/XC72 (0.20 mg_{Pt} cm^{-2} compared to 0.33 mg_{Pt} cm^{-2}). This highlights the efficiency of PtCo/MFCS in maximizing the utilization of platinum and achieving high catalytic activity even at reduced loadings, a critical factor for cost-effective and sustainable fuel cell technologies.

Moreover, the PtCo/MFCS MEA exhibits a lower HFR compared to the Pt/XC72 reference MEA. As widely reported in the literature [38], the HFR is strongly influenced by the interfacial contacts between MEA components as well as by the overall cell hydration. In the present case, the FESEM images in Fig. S1 show that the rougher electrode surface of the PtCo/MFCS catalyst layer provides improved physical contact with the membrane relative to the flatter morphology of the Pt/XC72-based electrode. This enhanced interfacial contact likely contributes to the reduced interfacial resistance, thereby further supporting the superior performance of the PtCo/MFCS MEA.

3.2.2. Material optimization

Once the superior performance of the non-commercial catalyst PtCo/MFCS over the commercial Pt/XC72 was established, the focus shifted to optimizing the ionomer to further enhance performance in the medium- and high-current density regions. Fig. 6(a–c) and (b,d) present the polarization curves and power curves in air at 100% RH and 80 °C, under ambient pressure and 2 bar absolute, respectively. Three different configurations were reported: MEA-ref, serving as a reference for both catalyst and ionomer; MEA 1, which uses non-commercial catalyst with a conventional ionomer; MEA 2, which employs the non-commercial catalyst with D79 as the ionomer.

Using D79 as the ionomer (MEA 2) enhances performance compared to MEA 1, where Nafion® is used. As shown in Fig. 6(a), this enhancement is particularly significant at ambient pressure in the medium- and high-current density regions, where ionic and diffusion resistances typically limit performance [46], while the kinetic performance remains comparable between the two samples. D79 enhances proton conductivity and catalyst layer integration due to its higher IEC and shorter proton transport pathways [47]. Moreover, the lower ionomer-to-carbon ratio promotes the formation of an optimized TPB [47], ensuring sufficient ionomer coverage for proton accessibility while maintaining adequate porosity for gas diffusion, thereby improving the electrochemical interface.

For completeness, Fig. S7(a) and (b) in the Supporting Information report the iR-corrected polarization curves for all MEAs measured at 80 °C and 100% RH under both 1 bar absolute and 2 bar absolute, respectively, enabling a direct comparison of the intrinsic performance differences among the samples.

The combination of the MFCS catalyst's higher intrinsic activity and the SSC ionomer's superior integration leads to reduced resistance and improved mass transport, which are critical for achieving high performance, especially under conditions where traditional Nafion®-based systems struggle.

These optimizations demonstrate that integrating a high-performing non-commercial catalyst like PtCo/MFCS with tailored ionomer properties can lead to substantial gains in fuel cell performance. This

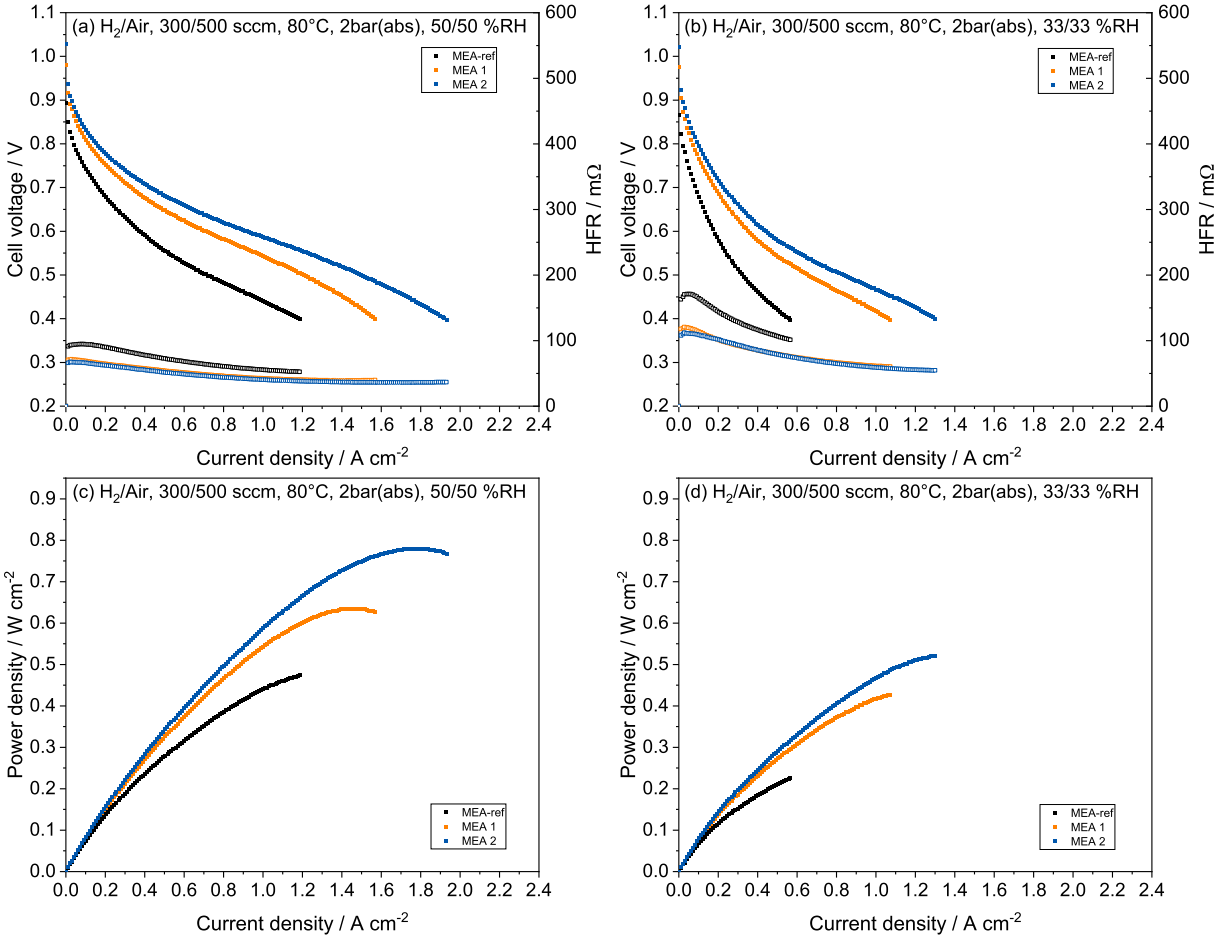

Fig. 7. Polarization curves and power curves recorded in H_2/air (300/500 sccm), at 80 °C and 2 bar absolute under (a, c) 50% RH and (b,d) 33% RH at both anode and cathode. The high-frequency resistance (HFR) is indicated on the right y-axis. MEA-ref (black line): Pt/XC72 (0.3 mg_{Pt} cm^{-2}), Nafion® ionomer (I/C 0.8), Nafion® 212. MEA 1 (orange line): PtCo/MFCS (0.2 mg_{Pt} cm^{-2}), Nafion® ionomer (I/C 0.8), Nafion® 212. MEA 2 (blue line): PtCo/MFCS (0.3 mg_{Pt} cm^{-2}), D79 ionomer (I/C 0.6), Nafion® 212. (For interpretation of the references to colour in this figure legend, the reader is referred to the Web version of this article.)

approach effectively addresses key challenges in catalyst utilization and resistance management, offering significant potential for improving efficiency across diverse operating regimes.

3.2.3. Variation of operating conditions

The analysis proceeded to evaluate performance across various operating conditions, recognizing the critical role that these conditions play in determining the size and complexity of the balance of plant (BoP), a key factor for heavy-duty applications. The resulting polarization curves for the different MEAs, measured at 33% and 50% RH at both anode and cathode, are reported in Fig. 7(a) and (b), respectively.

Compared to the fully humidified conditions reported in Fig. 6, the performance improvement of MEA 1 over MEA-ref is particularly evident under low-humidity conditions. This behavior is consistent with the presence of the nitrogen-doped MFCS support, which alters surface chemistry and water management within the catalyst layer. As evidenced by XPS results, despite a graphitization degree comparable to XC72, MFCS combines higher porosity with a greater density of polar surface functionalities, enhancing ionomer–support affinity, surface hydrophilicity, and local water retention. These features collectively account for the improved performance of PtCo/MFCS-based MEAs under dry operating conditions.

Such improvement is even more pronounced for MEA 2, where D79 is used instead of Nafion®. Owing to its shorter side chains, D79 exhibits superior water uptake capabilities, which helps to mitigate the effects of lower ambient humidity, further enhancing performance in dry environments.

It is also important to note that the HFR is strongly dependent on operating humidity, since membrane hydration and the water content within the catalyst layer directly influence ionic conductivity and contact resistance [38,48]. These effects are reflected in the HFR trends reported for the different MEAs and should be considered when interpreting the performance differences under varying RH conditions.

For completeness, Fig. S8(a) and (b) in the Supporting Information report the iR-corrected polarization curves for all MEAs measured at 80 °C and 2 bar absolute under both 33%RH and 50%RH, respectively, enabling a direct comparison of the intrinsic performance differences among the samples.

To provide a more practical basis for comparing the performance of the different MEAs, Fig. 8 reports the rated power at 0.67 V under varying operating conditions. Fixing the cell voltage for all samples ensures a comparison at equal cell efficiency relative to the theoretical thermodynamic value. Additionally, 0.67 V serves as a reference point for limiting heat production, making it a practical benchmark for assessing performance [49]. The analysis progressed from ambient pressure at 100% relative humidity to increased pressure at 2 bar absolute, with humidification levels of 100%, 50% and 33% (equal for both electrodes).

The MEA-ref, represented in black in Fig. 8, served as a baseline for comparison. Building on the previous insights into the advantages of the PtCo/MFCS catalyst and D79 ionomer, the analysis of rated power underscores how these materials deliver better performance compared to the MEA-ref under a range of operating conditions. At ambient pressure, the enhanced proton conductivity and optimized TPB resulting from the SSC ionomer configuration contribute significantly to better performance. Conversely, at higher pressures, the inherent driving force for electrochemical reactions mitigates mass transport limitations, making the improvements from tailored ionomer properties less pronounced.

The progressive reduction in humidification levels (100%, 50%, and 33% RH) further highlights the robustness of these MEAs. At both 100% and 50% RH, the D79-based MEA (MEA 2) clearly outperforms the Nafion®-based MEA (MEA 1), consistent with the superior water retention, higher proton conductivity, and thinner, more homogeneous nanofilms typically formed by SSC ionomers within the catalyst layer [33–35]. When the RH is reduced to 33%, the performance gap between the two electrodes becomes narrower; however, MEA 2 still maintains slightly higher performance over the entire current-density range. This convergence reflects the increasing influence of membrane dehydration at very low RH: because both MEAs employ the same Nafion® membrane, the membrane's protonic resistance becomes the dominant limitation, thereby dampening the intrinsic advantages provided by the D79 ionomer in the cathode CL.

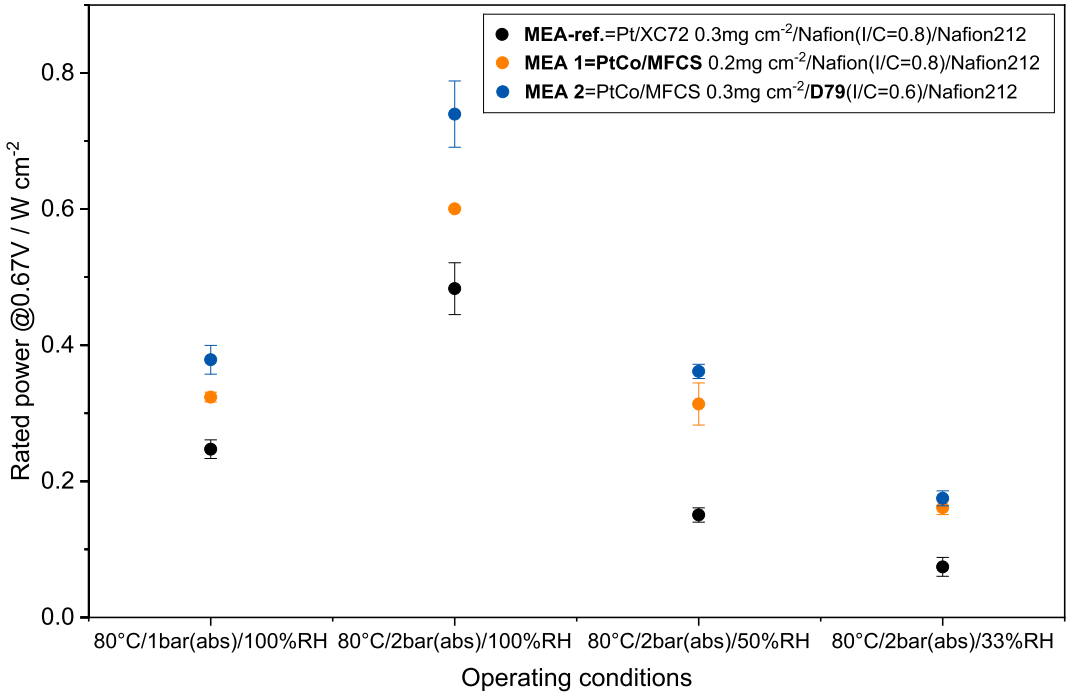

Fig. 8. Rated power (in mW cm^{-2}) at 0.67 V derived from polarization curves in H_2/air (300/500 sccm) for different samples under various operating conditions: from left to right, 80 °C/1 bar absolute/100% RH, 80 °C/2 bar absolute/100% RH, 80 °C/2 bar absolute/50% RH, 80 °C/2 bar absolute/33% RH.

Table 8
Summary of main results for the different MEAs tested, including ECSA analysis and, under various operating conditions, mass activity at 0.9 V, ohmic resistance and cathode charge transfer resistance (from EIS measured at 0.1 and 0.5 A cm^{-2}).

Sample	ECSA/m^2 g_{Pt}^{-1}	Operating conditions	H_2 crossover/mA cm^{-2}	Activity/mA mg_{Pt}^{-1}	R_{ohm}/Ω cm^2		$R_{ct,c}$/Ω cm^2	
				at 0.9 V	0.1 A cm^{-2}	0.5 A cm^{-2}	0.1 A cm^{-2}	0.5 A cm^{-2}
MEA-ref	48	80 °C/1 bar/100 %RH	0.44	–	0.096	0.087	0.37	0.39
		80 °C/2 bar/100 %RH	0.50	32	0.10	0.082	0.55	0.27
		80 °C/2 bar/50 %RH	0.51	–	0.24	0.19	0.94	0.32
		80 °C/2 bar/33 %RH	2.5	–	0.39	0.29	1.27	0.45
MEA 1	54	80 °C/1 bar/100 %RH	0.66	116	0.096	0.086	0.58	0.57
		80 °C/2 bar/100 %RH	0.88	537	0.092	0.081	0.48	0.20
		80 °C/2 bar/50 %RH	0.89	157	0.25	0.15	0.34	0.25
		80 °C/2 bar/33 %RH	2.1	67	0.41	0.30	0.53	0.35
MEA 2	50	80 °C/1 bar/100 %RH	0.43	99	0.088	0.089	0.39	0.15
		80 °C/2 bar/100 %RH	0.49	316	0.079	0.078	0.34	0.20
		80 °C/2 bar/50 %RH	0.75	99	0.22	0.18	0.37	0.20
		80 °C/2 bar/33 %RH	2.1	40	0.30	0.27	0.61	0.30

These results confirm that the PtCo/MFCS catalyst delivers superior rated power under a wide range of operating conditions, while also indicating that further improvements under extremely dry conditions may require concurrent optimization of both the catalyst-layer ionomer and membrane properties to fully exploit the benefits of SSC ionomer chemistry.

Table 8 summarizes the main results obtained for the different MEAs. While the ECSA values of the PtCo/MFCS-based samples are slightly higher than that of the Pt/XC72-based MEA, the difference in mass activity at 0.9 V is considerably more pronounced. Among the PtCo/MFCS-based MEAs, variations in mass activity are influenced by the catalyst loading, which increases from 0.20 mg_{Pt} cm^{-2} in MEA 1 to 0.30 mg_{Pt} cm^{-2} in MEA 2. This increase in loading leads to a reduction in mass-specific activity, due to a non-linear relationship between loading and electrochemical performances, as also reported by Heizmann et al. [45].

In addition, the hydrogen crossover values reported in Table 8 show comparable magnitudes across the different MEAs and follow consistent trends with operating conditions. As expected, an increase in hydrogen crossover is observed when the total pressure is increased, caused by the higher driving force for gas permeation across the membrane. Lower relative humidity also determines higher hydrogen crossover, as the reduced membrane hydration exhibits a denser but more rigid morphology with reduced water-filled pathways, which can facilitate the diffusion of small gas molecules such as hydrogen. Overall, the crossover values measured for the different MEAs are in line with each other and support the interpretation of the electrochemical trends discussed above.

Table 8 also reports some of the most relevant parameters extracted from the EIS fitting, namely the ohmic resistance (R_{ohm}) and the cathodic charge-transfer resistance ($R_{ct,c}$), for the different operating conditions and the investigated MEAs. To reliably extract these parameters and disentangle the contributions of electrode kinetics and mass-transport phenomena to the impedance response, the equivalent circuit model (ECM) originally proposed by Schöpen et al. [50] was employed. As illustrated in Fig. S9(a), the model consists of a series resistance (R_{ohm}), accounting for protonic and electronic transport through the membrane, electrodes, and current collectors, and two separate branches describing the anode and cathode processes. Each branch includes a charge-transfer resistance (R_{ct}) in parallel with a constant phase element (CPE_a), representing the double-layer capacitance of the catalyst layer. For the cathode branch, a finite-length Warburg diffusion element (W_s) was included, accounting for mass-transport effects under humidified conditions. This equivalent circuit provides an adequate description of all Nyquist spectra recorded under fully humidified conditions and for the majority of the operating points investigated. However, deviations from this behaviour are observed for measurements performed at 0.5 A cm^{-2} under reduced humidification conditions (50 % and 33 % RH). As the overall relative humidity decreases, the impedance response evolves significantly, revealing an additional low-frequency semicircle commonly associated with combined oxygen transport and proton conduction limitations within the partially dehydrated cathode catalyst layer. To accurately describe this additional process, a revised equivalent circuit was therefore implemented, as reported in Fig. S9(b) of the Supporting Information. It incorporates an additional transport-related branch, consisting of a mass-transport resistance (R_{mt}) and a Warburg-type element (W_{mt}) in parallel with a constant phase element (CPE_{mt}), placed in series with the conventional anode and cathode branches. This formulation enables accurate reproduction of the low-frequency arc and provides a physically meaningful representation of transport phenomena that become dominant under dry operating conditions.

A comprehensive overview of the EIS spectra and the corresponding equivalent-circuit fitting is provided in Fig. S10–S17 in the Supporting Information. The fitted parameters summarized in Table 8 reveal a clear and systematic increase in both ohmic resistance and charge-transfer resistances with decreasing relative humidity, in line with expectations related to membrane dehydration and increasing ion-transport limitations.

For completeness, Table S5 in the Supporting Information reports the R_{mt} values extracted from the revised ECM for measurements performed at 2 bar and 0.5 A cm^{-2} under 50% and 33% RH. The R_{mt} values for MEA 1 and MEA 2 are comparable at both humidity levels and are consistently lower than those of the reference MEA. This trend corroborates the conclusions drawn from the polarization and power-density curves, confirming that the PtCo/MFCS catalyst enables superior rated power over a broad range of operating conditions.

4. Conclusions

This study demonstrates the significant potential of rational catalyst–ionomer configuration and interface engineering to enhance the performance of PEMFCs in a materials-driven framework relevant to heavy-duty applications. The non-commercial PtCo catalyst supported on nitrogen-doped mesoporous carbon (PtCo/MFCS) outperformed the conventional Pt/Vulcan catalyst (Pt/XC72) in terms of both electrochemical surface area and mass activity, particularly under elevated pressure conditions. Beyond the kinetic region, performance improvements were also evident at medium and high current densities, owing to improved gas transport and enhanced water retention compared to Pt/XC72, especially under low-humidity conditions.

This improvement arises from a combination of the higher surface area provided by the MFCS carbon, more uniform and stable PtCo dispersion, and favorable catalyst–ionomer interactions associated with nitrogen functionalities in the carbon framework. Moreover, the optimized pore structure contributes to MEA performance by providing a balanced trade-off between oxygen transport and water retention, two processes that are typically in competition. These correlations are supported by complementary ex situ structural and physicochemical

characterizations, which provide direct insight into catalyst dispersion, support porosity, and catalyst–ionomer interfacial interactions, thereby enabling a mechanistic interpretation of the observed MEA-level performance trends.

The structural and transport-related features are further amplified when the catalyst is coupled with a SSC-PFSA ionomer (D79), especially under medium-to-high current densities. In this configuration, the ionomer is more evenly distributed across the support, and electrostatic interactions between the N-moieties and sulfonic acid groups mitigate the tendency of the short side chains to adsorb strongly on Pt, thereby preventing catalyst poisoning. The higher water retention of D79 improves performance under low-humidity conditions, but could theoretically lead to flooding under full humidification. However, the optimized pore distribution of PtCo/MFCS carbonaceous support enhances water management, maintaining performance and preventing flooding at high-humidity conditions. While our previous study reported that, using Pt/XC72 as the catalyst, D79-based MEAs underperformed Nafion®-based MEAs at 100% relative humidity due to flooding and transport limitations [36], the present work demonstrates that the synergy between PtCo/MFCS and SSC ionomer mitigates these limitations.

Overall, these results highlight how the deliberate combination of mesoporous nitrogen-doped carbon supports, alloy catalysts, and SSC ionomers can unlock synergistic performance gains that are often hindered when these components are studied independently. From a materials perspective, this approach establishes a clear and credible pathway toward meeting U.S. DOE targets for heavy-duty PEMFC systems, by simultaneously addressing kinetic activity, mass transport, and hydration management.

While the present work focuses on beginning-of-life performance-oriented understanding of the investigated materials and their synergistic interaction, future studies will extend this material platform toward durability assessment, scalability, and operation under more severe temperature and humidity conditions representative of heavy-duty operation regimes. Collectively, these findings provide a robust materials-level foundation for the development of high-performance MEAs enabling simplified BoP architectures and enhanced system robustness in next-generation zero-emission heavy-duty fuel cell vehicles.

Acronyms

BET	Brunauer- Emmett-Teller
BJH	Barrett-Joyner- Halenda
BoP	Balance of Plant
CL	Catalyst layer
CV	Cyclic voltammetry
D79	Aquivion® D79
DFT	Density functional theory
DOE	Department of Energy
ECM	Equivalent circuit model
ECSA	Electrochemical surface area
EDX	Energy Dispersive X-ray Spectroscopy
EIS	Electrochemical impedance spectroscopy
EW	Equivalent weight
FESEM	Field emission scanning electron microscope
GDL	Gas diffusion layer
HDV	Heavy-duty vehicle
HFR	High frequency resistance
HSA	High-surface-area
IEC	Ion exchange capacity
LDV	Light-duty vehicle
LSV	Linear sweep voltammetry
MEA	Membrane electrode assembly
MFCS	Multifunctional carbon support
OCV	Open circuit voltage
ORR	Oxygen reduction reaction
PEMFC	Proton exchange membrane fuel cell
PGM	Platinum group metal
PFSA	Perfluorosulfonic acid
PTFE	Polytetrafluoroethylene
RH	Relative humidity
SA	Surface area
SSC	Short side-chain
TEM	Transmission electron microscopy
TPB	Triple phase boundary
XPS	X-ray photoelectron spectroscopy
XRD	X-ray diffraction

(continued on next column)

(continued)

CRediT authorship contribution statement

Maria Chiara Massaro: Writing – original draft, Validation, Investigation, Formal analysis, Data curation. **Giovanni Marco Carrabba:** Investigation, Formal analysis, Data curation. **Enrico Sartoretti:** Visualization, Methodology, Formal analysis, Data curation. **Anna Ostroverkh:** Visualization, Data curation. **Fiora Artusio:** Methodology, Formal analysis, Data curation. **Roberto Pisano:** Visualization, Methodology. **Ulrike I. Kramm:** Writing – review & editing, Supervision, Resources, Methodology, Formal analysis, Data curation. **Alessandro Hugo Antonio Monteverde:** Writing – review & editing, Supervision, Funding acquisition, Formal analysis, Data curation, Conceptualization.

Declaration of competing interest

The authors declare that they have no known competing financial interests or personal relationships that could have appeared to influence the work reported in this paper.

Acknowledgements

The authors would like to acknowledge the support of pH Matter for providing the catalysts and sharing valuable information. They would also like to thank Leonardo S.p.A for funding M.C. Massaro's doctoral scholarship. Furthermore, the authors express their gratitude to Hendrik Haak, Pascal Theis, and all members of the Electrochemistry Group of Professor U. I. Kramm for their support during the testing phase. E. Sartoretti acknowledges the project PON Ricerca e Innovazione “REACT-EU” (DM 1062/21) funded by the Italian Ministero dell'Università e della Ricerca (MUR). This work was partially funded by the Ministero dell’Ambiente e della Sicurezza Energetica (MASE) and the Next Generation EU program (PNRR – M2C2, Investment Line 3.5) through the LightPEM project (Prog. n. RSH2A_000033 - CUP: F57G25000300006), as well as funding under the PNRR program (DM 352/22) through the “Next Generation EU” initiative of the European Union, is gratefully acknowledged. U. I. Kramm and A. Ostroverkh thank the German Research Foundation (DFG) for financial support through the gender inclusion funding of the spokesperson of CRC1487 Iron, upgraded! (grant no. 443703006).

Appendix A. Supplementary data

Supplementary data to this article can be found online at https://doi.org/10.1016/j.jpowsour.2026.239323.

Data availability

Data associated with the graphs related to in-situ electrochemical test are available via Zenodo: https://doi.org/10.5281/zenodo.18303487.

References

[1] H. Wang, R. Lin, X. Cai, S. Liu, D. Zhong, Z. Hao, Transition metal dissolution control in Pt-alloy catalyst layers for low Pt-loaded PEMFCs for improving mass transfer, Int. J. Heat Mass Tran. 178 (2021), https://doi.org/10.1016/j.ijheatmasstransfer.2021.121615.

[2] J. Martin, S. Küspert, K. Christmann, R. Marić, M. von Holst, H. Fadlullah, P. Elsässer, K.A. Friedrich, S. Vierrath, N. Zamel, A. Fischer, Templated N-Doped carbon nanospheres with tailored porosity for high performance PEM fuel cell catalysts under a wide range of conditions, Adv. Energy Mater. (2025), https://doi.org/10.1002/aenm.202500954.

[3] D.A. Cullen, K.C. Neyerlin, R.K. Ahluwalia, R. Mukundan, K.L. More, R.L. Borup, A. Z. Weber, D.J. Myers, A. Kusoglu, New roads and challenges for fuel cells in heavy-duty transportation, Nat. Energy 6 (2021) 462–474, https://doi.org/10.1038/s41560-021-00775-z.

[4] T.A.M. Suter, K. Smith, J. Hack, L. Rasha, Z. Rana, G.M.A. Angel, P.R. Shearing, T. S. Miller, D.J.L. Brett, Engineering catalyst layers for next-generation polymer electrolyte fuel cells: a review of design, materials, and methods, Adv. Energy Mater. 11 (2021), https://doi.org/10.1002/aenm.202101025.

[5] M. Chen, C. Zhao, F. Sun, J. Fan, H. Li, H. Wang, Research progress of catalyst layer and interlayer interface structures in membrane electrode assembly (MEA) for proton exchange membrane fuel cell (PEMFC) system, eTransportation 5 (2020), https://doi.org/10.1016/j.etran.2020.100075.

[6] O. Bethoux, Hydrogen fuel cell road vehicles: state of the art and perspectives, Energies 13 (2020), https://doi.org/10.3390/en13215843.

[7] Y.J. Wang, N. Zhao, B. Fang, H. Li, X.T. Bi, H. Wang, Carbon-Supported Pt-Based alloy electrocatalysts for the oxygen reduction reaction in polymer electrolyte membrane fuel cells: particle size, shape, and composition manipulation and their impact to activity, Chem Rev 115 (2015) 3433–3467, https://doi.org/10.1021/cr500519c.

[8] L. Ou, The origin of enhanced electrocatalytic activity of Pt-M (M = Fe, Co, Ni, Cu, and W) alloys in PEM fuel cell cathodes: a DFT computational study, Comput. Theor. Chem. 1048 (2014) 69–76, https://doi.org/10.1016/j.comptc.2014.09.017.

[9] H. Zhang, H.T. Chung, D.A. Cullen, S. Wagner, U.I. Kramm, K.L. More, P. Zelenay, G. Wu, High-performance fuel cell cathodes exclusively containing atomically dispersed iron active sites, Energy Environ. Sci. 12 (2019) 2548–2558, https://doi.org/10.1039/c9ee00877b.

[10] M. Kübler, S. Wagner, T. Jurzinsky, S. Paul, N. Weidler, E.D. Gomez Villa, C. Cremers, U.I. Kramm, Impact of surface functionalization on the intrinsic properties of the resulting fe–n–c catalysts for fuel cell applications, Energy Technol. 8 (2020), https://doi.org/10.1002/ente.202000433.

[11] R.K. Ahluwalia, X. Wang, L. Osmieri, J.-K. Peng, C.F. Cetinbas, J. Park, D.J. Myers, H.T. Chung, K.C. Neyerlin, Stability of atomically dispersed fe–n–c ORR catalyst in polymer electrolyte fuel cell environment, J. Electrochem. Soc. 168 (2021) 024513, https://doi.org/10.1149/1945-7111/abe34c.

[12] V. Gridin, M. Kübler, T. Hanstein, N. Heppe, N. Segura Salas, P. Theis, K. Hofmann, U.I. Kramm, Influence of the addition of nanoparticles on the oxygen reduction reaction characteristics of FeNC catalysts and the impact on the stability, J. Power Sources 561 (2023), https://doi.org/10.1016/j.jpowsour.2023.232713.

[13] A.H.A. Monteverde Videla, L. Osmieri, S. Specchia, Non-noble metal (NNM) catalysts for fuel cells: tuning the activity by a rational step-by-step single variable evolution, in: Electrochemistry of N4 Macrocyclic Metal Complexes: Volume 1: Energy, second ed., Springer International Publishing, 2016, pp. 69–102, https://doi.org/10.1007/978-3-319-31172-2_3.

[14] Hydrogen and Fuel Cell Technologies Office, DOE Technical Targets for Fuel Cell Systems and Stacks for Transportation Applications, (n.d.). https://www.energy.gov/eere/fuelcells/doe-technical-targets-fuel-cell-systems-and-stacks-transportation-applications (accessed November 23, 2023)..

[15] Y. Zeng, H. Zhang, Z. Wang, J. Jia, S. Miao, W. Song, Y. Xiao, H. Yu, Z. Shao, B. Yi, Nano-engineering of a 3D-ordered membrane electrode assembly with ultrathin Pt skin on open-walled PdCo nanotube arrays for fuel cells, J Mater Chem A Mater 6 (2018) 6521–6533, https://doi.org/10.1039/c7ta10901f.

[16] Y. Qiu, H. Zhang, H. Zhong, F. Zhang, A novel cathode structure with double catalyst layers and low Pt loading for proton exchange membrane fuel cells, Int. J. Hydrogen Energy 38 (2013) 5836–5844, https://doi.org/10.1016/j.ijhydene.2013.02.118.

[17] A. Salvatore Aricó, A. Stassi, I. Gatto, G. Monforte, E. Passalacqua, V. Antonucci, Surface properties of Pt and PtCo electrocatalysts and their influence on the performance and degradation of high-temperature polymer electrolyte fuel cells, J. Phys. Chem. C 114 (2010) 15823–15836, https://doi.org/10.1021/jp104528q.

[18] J. Peron, D. Edwards, M. Haldane, X. Luo, Y. Zhang, S. Holdcroft, Z. Shi, Fuel cell catalyst layers containing short-side-chain perfluorosulfonic acid ionomers, J. Power Sources 196 (2011) 179–181, https://doi.org/10.1016/j.jpowsour.2010.06.050.

[19] S.J. Hong, H.Y. Jung, S.J. Yoon, K.H. Oh, S.G. Oh, Y.T. Hong, D.M. Yu, S. So, Constrained hydrocarbon-based ionomers in porous Poly(tetrafluoroethylene) supports for enhanced durability of polymer electrolyte membrane fuel cells and water electrolyzers, J. Power Sources 551 (2022), https://doi.org/10.1016/j.jpowsour.2022.232221.

[20] J. Miyake, M. Kusakabe, A. Tsutsumida, K. Miyatake, Remarkable reinforcement effect in sulfonated aromatic polymers as fuel cell membrane, ACS Appl. Energy Mater. 1 (2018) 1233–1238, https://doi.org/10.1021/acsaem.7b00349.

[21] S. Holdcroft, Fuel cell catalyst layers: a polymer science perspective, Chem. Mater. 26 (2014) 381–393, https://doi.org/10.1021/cm401445h.

[22] K. Jiao, J. Xuan, Q. Du, Z. Bao, B. Xie, B. Wang, Y. Zhao, L. Fan, H. Wang, Z. Hou, S. Huo, N.P. Brandon, Y. Yin, M.D. Guiver, Designing the next generation of proton-exchange membrane fuel cells, Nature 595 (2021) 361–369, https://doi.org/10.1038/s41586-021-03482-7.

[23] R.L. Borup, A. Kusoglu, K.C. Neyerlin, R. Mukundan, R.K. Ahluwalia, D.A. Cullen, K.L. More, A.Z. Weber, D.J. Myers, Recent developments in catalyst-related PEM fuel cell durability, Curr. Opin. Electrochem. 21 (2020) 192–200, https://doi.org/10.1016/j.coelec.2020.02.007.

[24] E. Padgett, V. Yarlagadda, M.E. Holtz, M. Ko, B.D.A. Levin, R.S. Kukreja, J. M. Ziegelbauer, R.N. Andrews, J. Ilavsky, A. Kongkanand, D.A. Muller, Mitigation of PEM fuel cell catalyst degradation with porous carbon supports, J. Electrochem. Soc. 166 (2019) F198–F207, https://doi.org/10.1149/2.0371904jes.

[25] A. Cosenza, C. Roiron, G. Ferro, P. Atanassov, Nitrogen-doped carbon supports for Pt-based fuel cell electrocatalysts, Chem. Eng. J. 512 (2025), https://doi.org/10.1016/j.cej.2025.162816.

[26] S. Ott, F. Du, M.L. Luna, T.A. Dao, B.R. Cuenya, A. Orfanidi, P. Strasser, Understanding the performance increase of catalysts supported on N-Functionalized carbon in PEMFC catalyst layers, J. Electrochem. Soc. 169 (2022) 054520, https://doi.org/10.1149/1945-7111/ac6e4d.

[27] J. Ma, A. Habrioux, Y. Luo, G. Ramos-Sanchez, L. Calvillo, G. Granozzi, P. B. Balbuena, N. Alonso-Vante, Electronic interaction between platinum nanoparticles and nitrogen-doped reduced graphene oxide: effect on the oxygen reduction reaction, J Mater Chem A Mater 3 (2015) 11891–11904, https://doi.org/10.1039/c5ta01285f.

[28] S. Pylypenko, A. Borisevich, K.L. More, A.R. Corpuz, T. Holme, A.A. Dameron, T. S. Olson, H.N. Dinh, T. Gennett, R. O'Hayre, Nitrogen: unraveling the secret to stable carbon-supported Pt-alloy electrocatalysts, Energy Environ. Sci. 6 (2013) 2957–2964, https://doi.org/10.1039/c3ee40189h.

[29] A. Orfanidi, P. Madkikar, H.A. El-Sayed, G.S. Harzer, T. Kratky, H.A. Gasteiger, The key to high performance low Pt loaded electrodes, J. Electrochem. Soc. 164 (2017) F418–F426, https://doi.org/10.1149/2.1621704jes.

[30] S. Woo, S. Lee, A.Z. Taning, T.H. Yang, S.H. Park, S.D. Yim, Current understanding of catalyst/ionomer interfacial structure and phenomena affecting the oxygen reduction reaction in cathode catalyst layers of proton exchange membrane fuel cells, Curr. Opin. Electrochem. 21 (2020) 289–296, https://doi.org/10.1016/j.coelec.2020.03.006.

[31] S. Ott, A. Orfanidi, H. Schmies, B. Anke, H.N. Nong, J. Hübner, U. Gernert, M. Gliech, M. Lerch, P. Strasser, Ionomer distribution control in porous carbon-supported catalyst layers for high-power and low Pt-loaded proton exchange membrane fuel cells, Nat. Mater. 19 (2020) 77–85, https://doi.org/10.1038/s41563-019-0487-0.

[32] Y. Wang, D.F. Ruiz Diaz, K.S. Chen, Z. Wang, X.C. Adroher, Materials, technological status, and fundamentals of PEM fuel cells – a review, Mater. Today 32 (2020) 178–203, https://doi.org/10.1016/j.mattod.2019.06.005.

[33] S. Poojary, M.N. Islam, U.N. Shrivastava, E.P.L. Roberts, K. Karan, Transport and electrochemical interface properties of ionomers in low-pt loading catalyst layers: effect of ionomer equivalent weight and relative humidity, Molecules 25 (2020), https://doi.org/10.3390/molecules25153387.

[34] T. Li, J. Shen, G. Chen, S. Guo, G. Xie, Performance comparison of Proton exchange membrane fuel cells with nafion and aquivion perfluorosulfonic acids with different equivalent weights as the electrode binders, ACS Omega 5 (2020) 17628–17636, https://doi.org/10.1021/acsomega.0c02110.

[35] Y.C. Park, K. Kakinuma, H. Uchida, M. Watanabe, M. Uchida, Effects of short-side-chain perfluorosulfonic acid ionomers as binders on the performance of low Pt loading fuel cell cathodes, J. Power Sources 275 (2015) 384–391, https://doi.org/10.1016/j.jpowsour.2014.10.149.

[36] G.M. Carrabba, E. Sartoretti, E. Parisi, E. Simone, A.H.A. Monteverde, Carbon corrosion resistance in PEM fuel cells: comparative study of short and long side chain perfluorosulfonic acid ionomers, Int. J. Hydrogen Energy 133 (2025) 546–559, https://doi.org/10.1016/j.ijhydene.2025.04.262.

[37] M. Ocampo, P. Matter, C. Holt, A. Beutel, N. Casillas Giner, H. Xu, S. Zhong, G. Bender, C. Quesada, B. Pivovar, FY20 SBIR Phase IIA: Multi-Functional Catalyst Support, 2021.

[38] Y. Liu, M.W. Murphy, D.R. Baker, W. Gu, C. Ji, J. Jorne, H.A. Gasteiger, Proton conduction and oxygen reduction kinetics in PEM fuel cell cathodes: effects of ionomer-to-carbon ratio and relative humidity, J. Electrochem. Soc. 156 (2009) B970, https://doi.org/10.1149/1.3143965.

[39] N. Ramaswamy, S. Kumaraguru, R. Koestner, T. Fuller, W. Gu, N. Kariuki, D. Myers, P.J. Dudenas, A. Kusoglu, Editors' Choice—Ionomer side chain length and equivalent weight impact on high Current density transport resistances in PEMFC cathodes, J. Electrochem. Soc. 168 (2021) 024518, https://doi.org/10.1149/1945-7111/abe5eb.

[40] T. Soboleva, X. Zhao, K. Malek, Z. Xie, T. Navessin, S. Holdcroft, On the micro-, meso-, and macroporous structures of polymer electrolyte membrane fuel cell catalyst layers, ACS Appl. Mater. Interfaces 2 (2010) 375–384, https://doi.org/10.1021/am900600y.

[41] A. Patel, K. Artyushkova, P. Atanassov, V. Colbow, M. Dutta, D. Harvey, S. Wessel, Investigating the effects of proton exchange membrane fuel cell conditions on carbon supported platinum electrocatalyst composition and performance, J. Vac. Sci. Technol. A: Vacuum, Surfaces, and Films 30 (2012), https://doi.org/10.1116/1.4707153.

[42] K. Wan, H. Chen, J. Wang, B. Li, M. Chai, P. Ming, C. Zhang, Coupling atomically ordered PtCo catalysts with ultrathin nitrogen-doped carbon shell for enhanced oxygen reduction, J. Catal. 427 (2023), https://doi.org/10.1016/j.jcat.2023.115124.

[43] Z. Ni, L. Wang, B. Wang, Unveiling the impact of pore structure of cathode catalyst layer on proton exchange membrane cell performance, Int. J. Hydrogen Energy 60 (2024) 1404–1413, https://doi.org/10.1016/j.ijhydene.2024.02.303.

[44] E. Hornberger, T. Merzdorf, H. Schmies, J. Hübner, M. Klingenhof, U. Gernert, M. Kroschel, B. Anke, M. Lerch, J. Schmidt, A. Thomas, R. Chattot, I. Martens, J. Drnec, P. Strasser, E. Hornberger, Impact of carbon N-Doping and Pyridinic-N content on the fuel cell performance and durability of carbon-supported Pt nanoparticle catalysts, ACS Appl. Mater. Interfaces 14 (2022) 18420–18430, https://doi.org/10.1021/acsami.2c00762.

[45] P.A. Heizmann, H. Nguyen, M. von Holst, A. Fischbach, M. Kostelec, F.J. Gonzalez Lopez, M. Bele, L. Pavko, T. Đukić, M. Šala, F. Ruiz-Zepeda, C. Klose, M. Gatalo, N. Hodnik, S. Vierrath, M. Breitwieser, Alternative and facile production pathway towards obtaining high surface area PtCo/C intermetallic catalysts for improved PEM fuel cell performance, RSC Adv. 13 (2023) 4601–4611, https://doi.org/10.1039/d2ra07780a.

[46] M. Arif, S.C.P. Cheung, J. Andrews, A systematic approach for matching simulated and experimental polarization curves for a PEM fuel cell, Int. J. Hydrogen Energy 45 (2020) 2206–2223, https://doi.org/10.1016/j.ijhydene.2019.11.057.

[47] H. Ren, Y. Teng, X. Meng, D. Fang, H. Huang, J. Geng, Z. Shao, Ionomer network of catalyst layers for proton exchange membrane fuel cell, J. Power Sources 506 (2021), https://doi.org/10.1016/j.jpowsour.2021.230186.

[48] Y. Qi, Y. Huang, Z. Gao, C.H. Chen, A. Perego, H. Yildirim, M. Odgaard, T. Asset, P. Atanassov, I.V. Zenyuk, Insight into carbon corrosion of different carbon supports for Pt-based electrocatalysts using accelerated stress tests in polymer electrolyte fuel cells, J. Power Sources 551 (2022), https://doi.org/10.1016/j.jpowsour.2022.232209.

[49] V. Yarlagadda, M.K. Carpenter, T.E. Moylan, R.S. Kukreja, R. Koestner, W. Gu, L. Thompson, A. Kongkanand, Boosting fuel cell performance with accessible carbon mesopores, ACS Energy Lett. 3 (2018) 618–621, https://doi.org/10.1021/acsenergylett.8b00186.

[50] O. Schopen, S. Narayan, M. Beckmann, A.U.H. Najmi, T. Esch, B. Shabani, An EIS approach to quantify the effects of inlet air relative humidity on the performance of proton exchange membrane fuel cells: a pathway to developing a novel fault diagnostic method, Int. J. Hydrogen Energy 58 (2024) 1302–1315, https://doi.org/10.1016/j.ijhydene.2024.01.218.